

Trinity: Liberty University Rocketry Team

Team 134 Project Technical Report to the 2025 International Rocket Engineering Competition

Luke Krick¹

Liberty University, Lynchburg, Virginia, 24515, U.S.A

Simon Babcock²

Liberty University, Lynchburg, Virginia, 24515, U.S.A

Johnny Sugarman³

Liberty University, Lynchburg, Virginia, 24515, U.S.A

Sam Worthington⁴

Liberty University, Lynchburg, Virginia, 24515, U.S.A

Rachel Phillips⁵

Liberty University, Lynchburg, Virginia, 24515, U.S.A

Price Drawdy⁶

Liberty University, Lynchburg, Virginia, 24515, U.S.A

Derek Works⁷

Liberty University, Lynchburg, Virginia, 24515, U.S.A

¹ Chief Engineer, LU School of Engineering, 1971 University Blvd Lynchburg VA 24515

² Project Manager, LU School of Engineering, 1971 University Blvd Lynchburg VA 24515

³ Manufacturing Lead, LU School of Engineering, 1971 University Blvd Lynchburg VA 24515

⁴ Aerostructures Team Lead, LU School of Engineering, 1971 University Blvd Lynchburg VA 24515

⁵ Recovery Team Lead, LU School of Engineering, 1971 University Blvd Lynchburg VA 24515

⁶ Avionics and Payload Team Lead, LU School of Engineering, 1971 University Blvd Lynchburg VA 24515

⁷ Propulsion Team Lead, LU School of Engineering, 1971 University Blvd Lynchburg VA 24515

I. Nomenclature

F	=	Force
C_k	=	Coefficient of Shock
C_d	=	Coefficient of Drag
ρ	=	Density of air
v	=	Velocity
R_m	=	Mass Ratio
S_{sd}	=	Surface Area
m	=	Mass
σ_f	=	Flexural Stress
L	=	Length of Sample
b	=	Width of Sample
d	=	Depth of Sample
ϵ_f	=	Flexural Strain
w_0	=	Flexural Displacement
E	=	Modulus of Elasticity
I	=	Second Moment of Area

II. Abstract

The Liberty University Rocketry Team's third high-power rocket, Trinity, is designed to compete in the 10K COTS category of the Intercollegiate Rocket Engineering Competition (IREC). This vehicle aims to improve our methodology from last year and establish new precedents for the research our team plans to conduct as we learn and grow as a team. Each critical component of Trinity's construction has been through rigorous testing and experimentation to establish a methodology for future generations of this team to continue experimenting and expanding upon their engineering design process. Furthermore, Trinity has several experiments on board, namely our custom remote camera activation electronics and our experimental payload that is designed to predict rocket apogee through AI model training.

III. Mission Concept of Operations Overview (Introduction)

The Liberty University Rocketry Team is the official rocketry competition team of Liberty University – a private Christian four-year institute in Lynchburg, Virginia. Our team is composed of 56 passionate students from a few different majors. The team is mostly composed of mechanical engineering students; however, the team also has several electrical engineering and computer science students. On top of that, the team has members from non-engineering majors who help with media and some advanced coding languages. Because our team is an official competition team of Liberty University School of Engineering (LUSE) it is under the tutelage and oversight of the LUSE Competition Team Program Director, Mr. Steve Mason and is funded by and representative of LUSE.

Our team is composed of 4 sub-teams: Aerodynamics, Avionics/Payload, Propulsion, and Recovery. The Aerodynamics sub-team is responsible for the engineering design decisions concerning all exterior components of the rocket, including the airframe material, fins, and paint. Unlike most teams, our Payload sub-team is not only responsible for the experimental payload, but also the recovery electronics, thus we have named this team "Avionics/Payload". Our Propulsion sub-team is responsible for all decisions concerning the motor and its mounting hardware. Finally, our Recovery sub-team is responsible for all parachute deployment operations outside of electronics.

Each of these sub-teams is guided by a Sub-team Lead, and the Sub-team Leaders are directed and coordinated by the Chief Engineer. The Chief Engineer is responsible for confirming all major design decisions and is required to understand every element of the rocket to prevent possible design conflicts between the different sub-systems. In addition to these leadership roles, the team also has an appointed Project Manager and Manufacturing Lead. The team

Project Manager handles all logistical matters including test launch dates, possible corporate donors, community outreach events, and competition travel logistics. The Manufacturing Lead is responsible for determining the best possible way to manufacture the various rocket components and ensuring proper safety protocols are followed in our manufacturing workspace. The students on our team are also guided by our team's advisor and mentor, Mark Miller.

Our team's chain of command is depicted in the image below (Fig. 1). Furthermore, our team seeks to avoid fourth year/senior students being in direct leadership for the sake of ensuring the transfer of knowledge and sustainability of the team from year to year. It is preferred that Team Leads are not older than third year/junior year in their degree. Each one of the team leaders have agreed to abide by this chain of command and their various responsibilities as established in our team constitution.

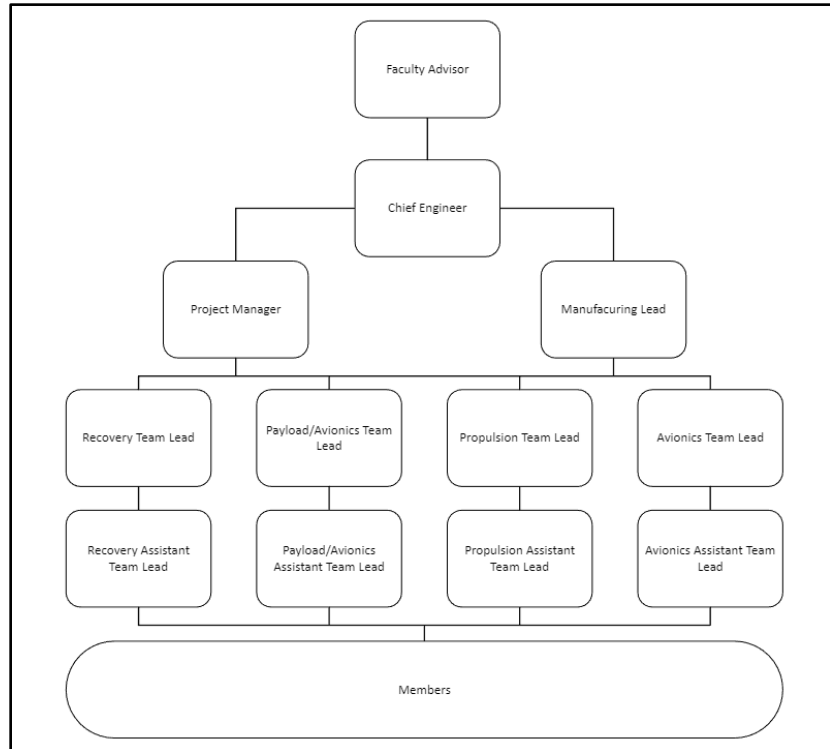


Fig. 1: Leadership Structure Diagram

Top-Level Overview

The Trinity Rocket is our second competition rocket for the 10K COTS category. Standing at 135 inches tall and weighing about 54 pounds, Trinity is designed to reach an altitude of 10,000ft AGL in just under 25 seconds. Over the past two semesters, the 56 students on our team have worked diligently to make this one of the best student-built rockets in the world.

The body of the rocket has a 6-inch inner diameter and is composed largely of carbon fiber except for the fiberglass nosecone. The fins are also made of carbon fiber and are optimized with a modified Clipped-Delta shape. Trinity is propelled by an Aerotech M1845NT-PS which is an ammonium-perchlorate based solid fuel. The internals of the rocket consist of an experimental payload, avionics bay, long range GPS, and both a drogue and main recovery system. The experimental payload is in CubeSat dimensions (10cm x 10cm x 40cm) and is designed to test cooling electronics. The avionics bay consists of a main and redundant RRC3 altimeter which use barometric data to accurately determine altitude. In addition to these altimeters, the avionics bay also contains custom electronics for remote camera activation. The rocket nosecone houses a long-range Featherweight GPS to aid the recovery process after touchdown. The 24in elliptical drogue chute will deploy at the rocket's apogee when expanding gases raise internal pressure and shear the connecting pins because of black powder ignition. The 96in toroidal main chute is deployed in a similar fashion at 1,200ft AGL on descent.

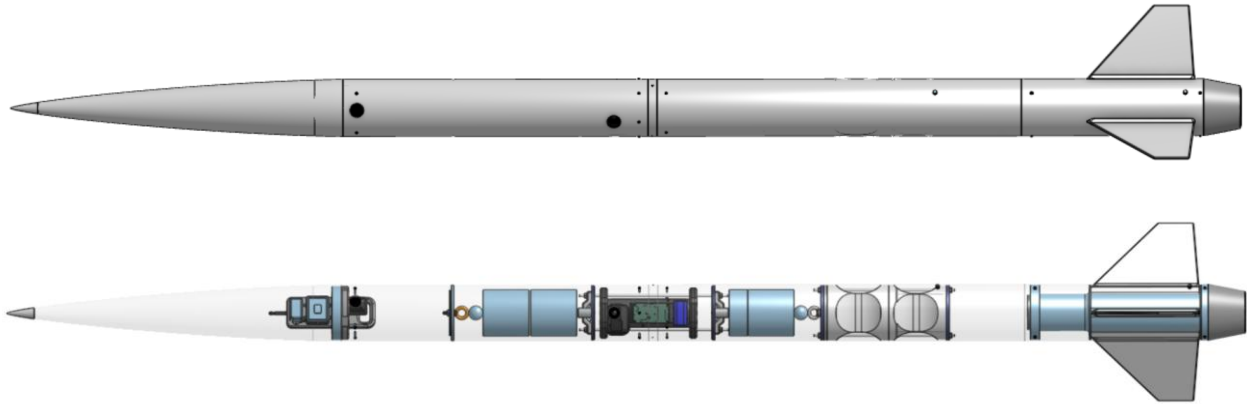


Fig. 2: CAD of Trinity

Propulsion Subsystems

I. Subsystem Overview

The propulsion system is responsible for providing the thrust that propels the rocket to apogee. It consists primarily of fuel, a nozzle, a casing, and support hardware. The motor for Trinity's competition launch is an AeroTech M1845NT-PS, which comes with a converging/diverging nozzle. The casing is an AeroTech RMS-98/7680 high power motor reload kit which is designed to work with the M1845 motor. Trinity uses an aluminum retaining ring on the exterior of the motor tube to secure the motor. The rocket motor mount tube is held in the center of the rocket by G10 fiberglass centering rings.

II. Motor Selection

Two years ago, Liberty Rocketry used a Cesaroni M1590 motor, but several changes led to choosing the AeroTech M1845. First, Cesaroni was suffering from a motor shortage, so AeroTech was determined to be the more reliable manufacturer for this semester. The M1845 simulated closer to 10,000ft more than any other motor on OpenRocket, which is the primary simulation software used by Liberty Rocketry. Unfortunately, because of supply chain issues, the motor had to be ordered before all the rocket components were available to be weighed for more accurate simulations. Thus, it was a high priority that the chosen motor was simulating very close to 10,000ft with additional margin so that the inevitable weight changes do not prohibit the final rocket from reaching the desired target of 10,000ft. Several other AeroTech motors were simulated, but none of them gave much margin of error. Therefore, the AeroTech M1845 was chosen for its availability and its simulated performance. Choosing this motor represents one of the foundational design decisions that the rest of the rocket is designed around.

III. Motor Diameter Difference

The team conducted a test launch to approximately half of the goal altitude using a 75mm motor (L1420) to test subsystem functionality and ensure proper functionality of the recovery system with less risk than a full-scale launch. To allow the rocket to launch using a significantly smaller motor than it was designed for, a set of aluminum adapter rings were fitted around the smaller casing to ensure a secure fit in the motor tube. For the full-scale launch, a 98mm M1845 motor will be used to reach an apogee of around 10,000ft.

IV. Test Launch Goals and Results

The first test launch primarily served as testing for the recovery system and to help calibrate the aerodynamics of our simulations. Our first sub-scale launch came within 1.07% of the predicted apogee of 5079 feet by reaching

5134 feet. The first test launch featured an unwrapped rocket with some slight differences from the final weight, so a second test launch is scheduled. This test launch will be full scale and body-wrapped, so it will be used to further calibrate the simulations of the rocket, allowing the team to make minor adjustments to the weight of the rocket to tune Trinity to as close as possible to 10,000ft.

V. Manufacturing Process

5.1 Motor Tube Manufacture

The propulsion sub-team marked the locations on the motor tube of each centering ring. To ensure the rings stayed in place during epoxying, tape was wrapped along the bottom of these lines to create a resting surface. The inside of each of the centering rings was then sanded until they all fit securely over the cardboard motor mount, making sure they were sanded evenly to preserve concentricity. Epoxy and hardener were mixed in a 1:1 weight ratio with chopped fiberglass epoxy filler added until the mixture reached the desired viscosity to minimize the effect of gravity on the shape of the fillets. Then, this epoxy mixture was used to create fillets on the untaped sides of the centering rings, securely bonding them to the cardboard tubing. This process ensured proper alignment and structural integrity for the motor mount assembly.



Fig. 3: Motor Tube before Assembly

5.2 Motor Tube Installation

Once the fillets on the first side were fully cured, the tape was carefully removed from the other side and fillets were applied there as well. Then, standing the cardboard tube upright as it would be in the lower section of the rocket body, a bead of epoxy was applied to the outside of the rings before sliding the cardboard tubing into the aft

side of the main body tubing. No epoxy fillets were placed between the aft and the middle centering ring so that the fins were not obstructed.

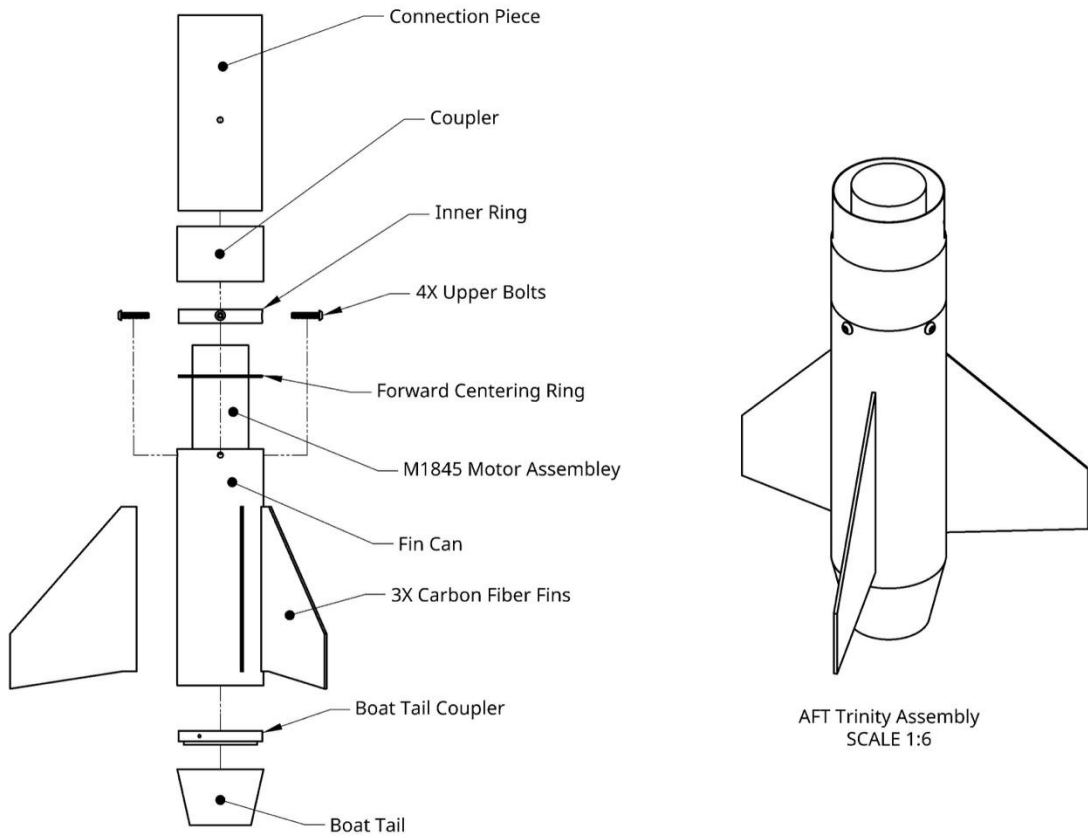
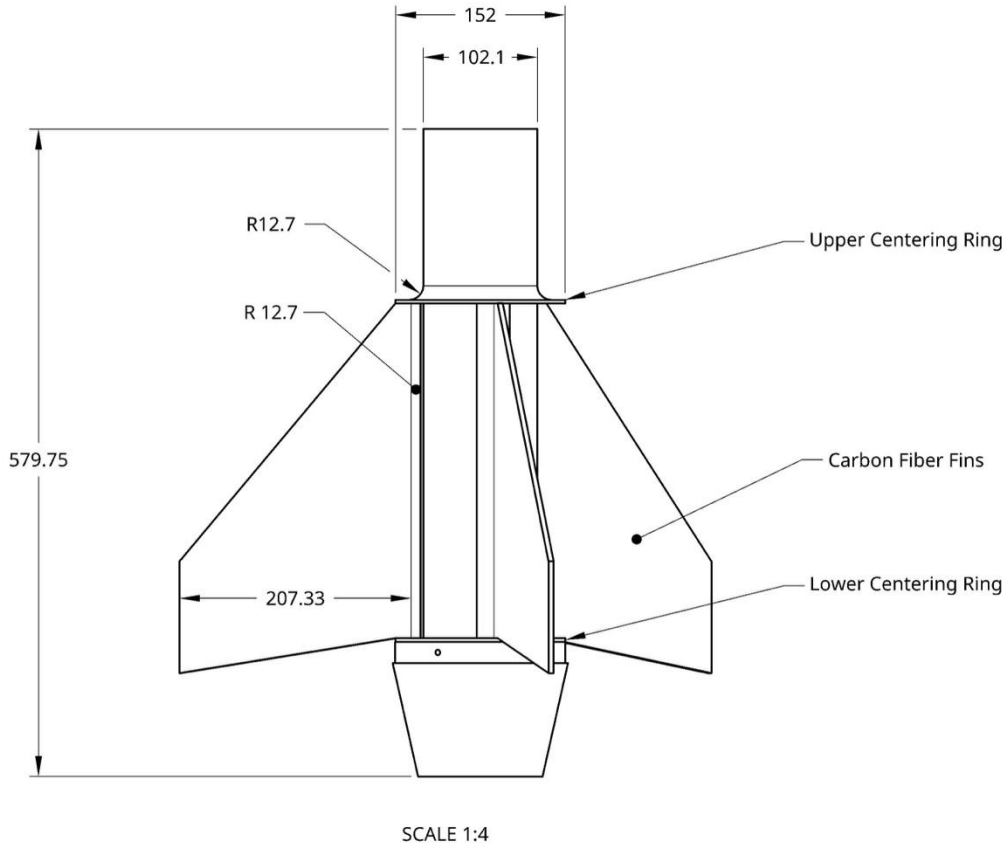


Fig. 4: CAD of the Fincan



note. All Dimensions are in millimeters

Fig. 5: Dimensions of the Fincan

5.3 Fin Can

If a fin is damaged during a launch, it would be extremely difficult to repair the fin while keeping the rest of the rocket intact. The team decided to avoid this potential problem by integrating the fins into a removable sheath. This fin can is secured to the rocket using bolts, allowing for easy replacement in case of damage.

For bolt shear calculations, the ultimate tensile strength (*UTS*) of the steel was provided by the manufacturer as 70,000 psi. Following standard industry assumptions, the ultimate shear strength (*USS*) was approximated using the following relationship:

$$USS \approx 0.6 \cdot UTS = 42,000 \text{ psi} \approx 289.6 \text{ MPa} \quad (1)$$

The shear force *V* experienced by each of the three evenly spaced bolts was determined from the OpenRocket simulation to determine the acceleration of the fin can during recovery deployment:

$$V = \frac{ma}{N} = \frac{10.31 \text{ kg} \cdot 216.11 \frac{\text{m}}{\text{s}^2}}{3 \text{ bolts}} = 742.7 \frac{\text{N}}{\text{bolt}} \quad (2)$$

The maximum shear stress experienced across a circular cross section is given by the following formula, where the minor diameter of the 8-32 bolts *d* is 0.1300 inches and the area is doubled because the bolt is experiencing dual shear:

$$\tau_{max} = \frac{4V}{3A} = \frac{4V}{3\left(2\frac{\pi}{4}d^2\right)} = 37,303.16 \text{ Pa} \quad (3)$$

The factor of safety (FOS) is calculated using the following relationship:

$$FOS = \frac{USS}{\tau_{max}} = 7,762.88 \quad (4)$$

As shown by Eq. 4, the factor of safety is sufficiently high that even given the approximation used for the *USS* there can be a high degree of confidence that the fin can attachment screws will not fail during recovery.

5.4 Boat Tail

Compared to last year, this year's rocket is heavier and would therefore need a larger engine to reach the same altitude. To avoid buying a larger casing, a boat tail was used to reduce pressure drag caused by low pressure regions behind the rocket. The boat tail guides the airflow smoothly from the rocket body to freestream air. This causes less of a pressure difference between the front and rear section. This allowed the team to use the same engine that was used last year.

A 3D-printed ring with brass heat-set threaded inserts was used to secure the boat tail to the airframe. The ring mount is epoxied to a 3D-printed negative of the boat tail, which is in turn epoxied to the carbon-fiber boat tail. This assembly is secured to the airframe by running bolts through the airframe into the threaded inserts in the upper ring.

For the bolt shear calculations, the same formulas and methodology applied to the fin can bolt shear calculations were utilized, except that these only experienced single shear and 6-32 bolts were used that had a minor diameter of 0.1040 inches. These calculations gave an FOS of 2,484, which shows that there can also be a high degree of confidence that the boat tail screws will not fail.

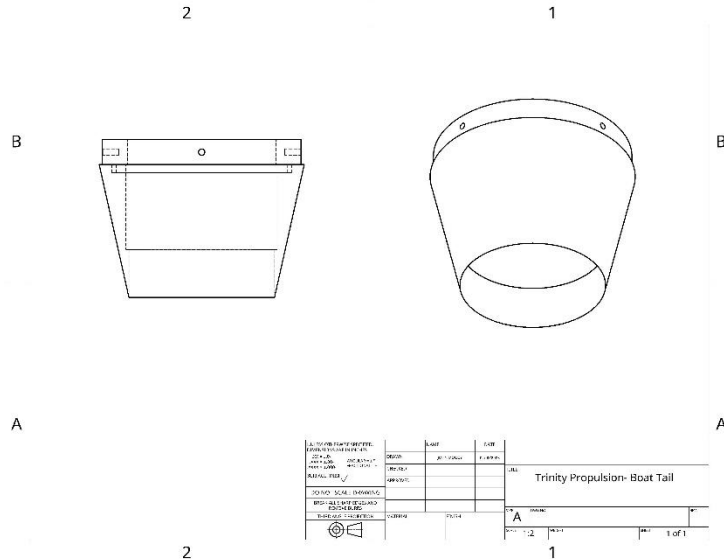


Fig. 6: Technical Drawing of the Boattail

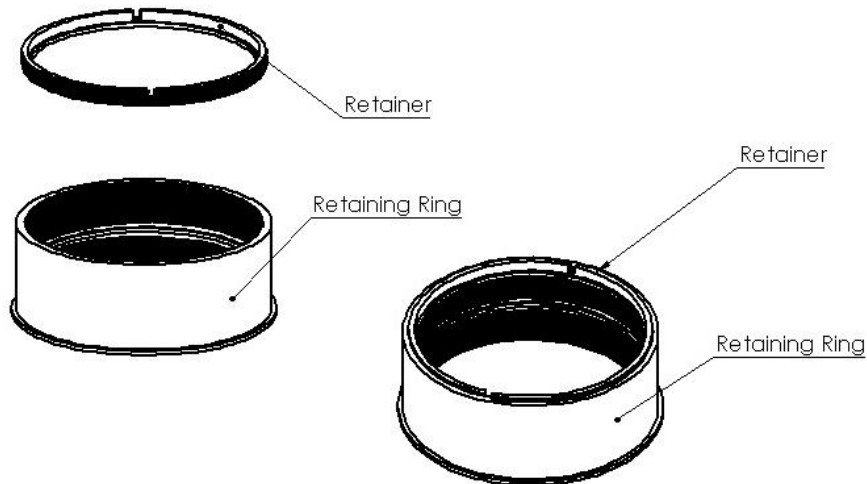


Fig. 7: Motor Retainer Diagram

Aero-structures Subsystems

I. Subsystem Overview

This subsystem consists of the nosecone, the airframe, the fin can, and the boat tail. Each of these components will have corresponding engineering drawings in the relevant appendix. These components all influence the aerodynamic characterization of the rocket, a topic of upmost importance in a competition such as the Intercollegiate Rocket Engineering Competition (IREC) where teams attempt to design rockets that come as close as possible to the desired apogee, in our case 10,000ft. The following sections will outline our team's approach to and execution of the design and manufacturing of the aero-structures subsystem.

II. Design Philosophy

At the earliest stages of Trinity's design, the team's leadership worked to establish goals, constraints, and variables that would guide the development and design of Trinity. These goals serve as targets that the team aims to achieve in the development of the entire rocket system regarding the aerodynamics of the rocket. These goals included designing and manufacturing an aero-structure subsystem that successfully integrates as intended with all other rocket components and entirely complies with competition rules, be within 3% of our target apogee of 10,000 feet at the competition launch, be within 5% of our simulated apogee for all launches (including test launches and competition), have a full CAD model as it pertains to the aero-structures subsystem by the time manufacturing begins, and create decision matrices backed by simulated and experimental data to justify design decisions for each component within the subsystem. The single most important goal of the aero-structures subsystem is to design the rocket to reach an apogee as close as possible to 10,000 feet. These goals influence many different key aspects of Trinity's design. For example, our goal to be within 3% of each simulated launch apogee means that our team needs to develop the physical components in such a way that the resulting flight is accurate and repeatable while also making sure that our predictive models accurately represent the real flight so that they can be confidently used to predict the flight behavior at competition.

Another aspect of the design philosophy is the generation and use of constraints and requirements. For our purposes, constraints can be understood as either quantifiable or Boolean objectives that must be met per competition rules or regulations. Requirements are objectives that are self-imposed and may not be quantifiable. Some of the constraints or requirements are taken from the goals expressed above. They are as follows:

Table 1: Constraints and Requirements

Constraints	Requirements
C.1 – Must include space for 10cm x 10cm x 40cm payload	R.1 – Successful integration with other rocket systems
C.2 – Static stability margin between 1.5-4 calibers at all flight speeds	R.2 – Enough internal volume for recovery, avionics, and propulsion subsystems
C.3 – Cannot use PVC, PML Quantum Tube, stainless steel on any airframe structure	R.3 – Expenses within allotted budget
C.4 – Utilizes custom or COTS components	R.4 – Apogee within 3% of 10,000 feet target apogee
C.5 – Apogee within 30% of 10,000 feet	

The team is then able to investigate how different variables impact these constraints and requirements. Examples of these variables include airframe length, airframe thickness, fin height, fin thickness, nosecone geometry, etc. The design process consists of evaluating the many different relationships that altering these variables have on the desired objectives. Broadly speaking, the aero-structures subsystem can be split into the nosecone, airframe, and fins. These are the main components that will be interacting with and directing the airflow around the rocket. Each of these sections will have its own discussion section with further discussion on the details of the design process.

III. Aero-structures Design Process

3.1 Nosecone Design Process

The primary variables to consider for the nosecone design process are the aerodynamic shape, the final outer diameter, and the material. The final diameter of the nosecone is dependent on the size of the airframe in order to create a continuous surface. The airframe inner diameter was chosen to be 6", the reasoning for which will be discussed in section 3.2. To ensure that there are minimal discontinuities in the rocket body, the nosecone should match the size of the airframe as closely as possible. Therefore, the team only considered 6" diameter nosecones.



Fig. 8: Static Pressure Contour for VKH Nosecone

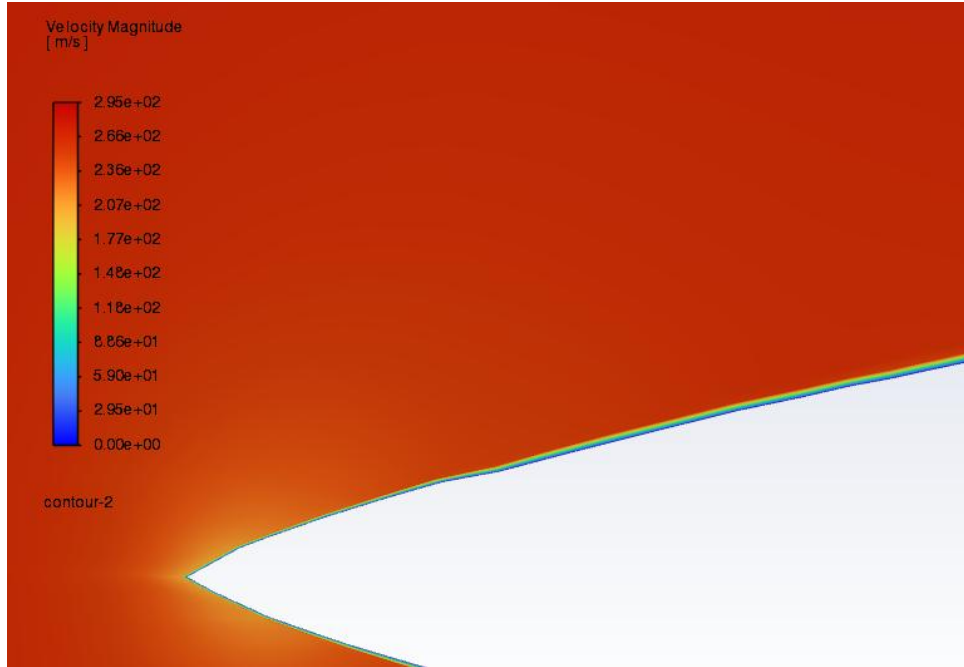


Fig. 9: Velocity Magnitude Contour for VKH Nosecone

The next nosecone variable to consider is geometry. Because our team does not have the capacity to fabricate our own nosecone, the team is limited to what is commercially available. These options include conical, Haack, and ogive geometries. A comprehensive literature review was conducted on these different shapes to identify the relative strengths and weaknesses of the different geometries. Trinity will never exceed the transonic velocity range, with the latest simulations showing a peak around 0.823 Mach. At these velocities, the geometry is not as influential as it would be at supersonic velocities; however, various geometries will still result in noticeably different flight results. Unfortunately, the available nosecone selection options are limited based on which geometries are commercially available. Of the potential options, the Von Karman Haack (VKH) geometry was chosen. It is a mathematically derived geometry, optimized to produce the minimum drag at a given length and diameter. It was found to be commercially available in a 6" end diameter.

To validate this choice, we also performed a computational fluid dynamics (CFD) simulation. This simulation yielded pressure contours shown in figure 6 display a pressure concentration at the nosecone tip and lower pressures along the rear edges. This makes sense as it mirrors the behavior of a wing, which has high pressure in the front, and lower pressure along the top and bottom edges, with the lowest at the top providing lift. The disturbance thickness boundary layer is shown in Figure 7. Due to the high speed of the surrounding fluid, the boundary layer is very small, so the contour plot is focused on the nosecone area.

Another aspect of nosecone geometry is the fineness ratio, which is the ratio of the length of the nosecone to its base diameter. Generally, as the fineness ratio increases, the wake drag decreases but the skin friction drag increases. The team's literature review reported that a fineness ratio of 5:1 represents the optimal balance between the wake drag and frictional drag for our purposes. Due to its good properties, the 5:1 ratio is commonly sold by vendors; therefore, the team decided to choose a 5:1 Von Karman nosecone.

The final consideration for the nosecone is the material selection. This decision is tied both to the commercially available selection and the properties of the chosen material. The first important property is radio frequency (RF) transparency. To allow the rocket and ground station to communicate with the GPS and onboard camera system, some portion of the rocket must be RF transparent. The airframe was chosen to be carbon fiber as is discussed in section 3.2, so the nosecone must be made of some RF-transparent material. Fiberglass, a common material for nosecone construction, is RF transparent, allowing the team to mount the communication antenna in the nosecone and have reliable communication through the fiberglass. Secondly, the material must be strong enough to withstand any force

applied to it over the course of its use. The forces from the air throughout the launch and flight would be much lower than the force of landing, so the force experienced upon landing was calculated using the equations below.

$$F = \frac{4}{3} E^* R^{\frac{1}{2}} d^{\frac{3}{2}} \quad (5)$$

$$E^* = \left(\frac{1 - \nu_1^2}{E_1} + \frac{1 - \nu_2^2}{E_2} \right)^{-1} \quad (6)$$

$$d = \frac{2.2 \rho^{\frac{2}{5}} R U_0^{\frac{4}{5}}}{E^{*\frac{2}{5}}} \quad (7)$$

Here, F is the force on the airframe, R is the radius of the tube, d is the distance into the surface the tube is compressed, E^* is the effective modulus of elasticity, ν is Poisson's ratio for each material, E is the elastic modulus of each material, ρ is the density of the tube, and U_0 is the velocity of the tube immediately before impact. This calculation mainly represents only the order of magnitude the nosecone may experience due to the heavy dependency upon the terrain properties and the orientation with which the nosecone would strike the ground. However, the worst case was assumed for terrain and falling orientation calculations. This led to a force of 369 lbf. This value was then used in a finite element analysis (FEA) simulation to validate the nosecone's ability to withstand the force of landing.

Figure 8 shows the results of the simulation with a deformation scale of 152. It exhibits a maximum pressure of only 6.17 ksi with a factor of safety (FOS) of 37, so the approximation and risk involved are acceptable. Additionally, all past rockets made by our team have used fiberglass nosecones, and never have we experienced any structural damage. Alternatively, carbon fiber (CF) was considered, but due to the lack of RF transparency, it was discounted because its inclusion would necessitate a total redesign of the rocket communication system. For these reasons, the team chose to select a 5:1 Von Karman Fiberglass nosecone for Trinity.

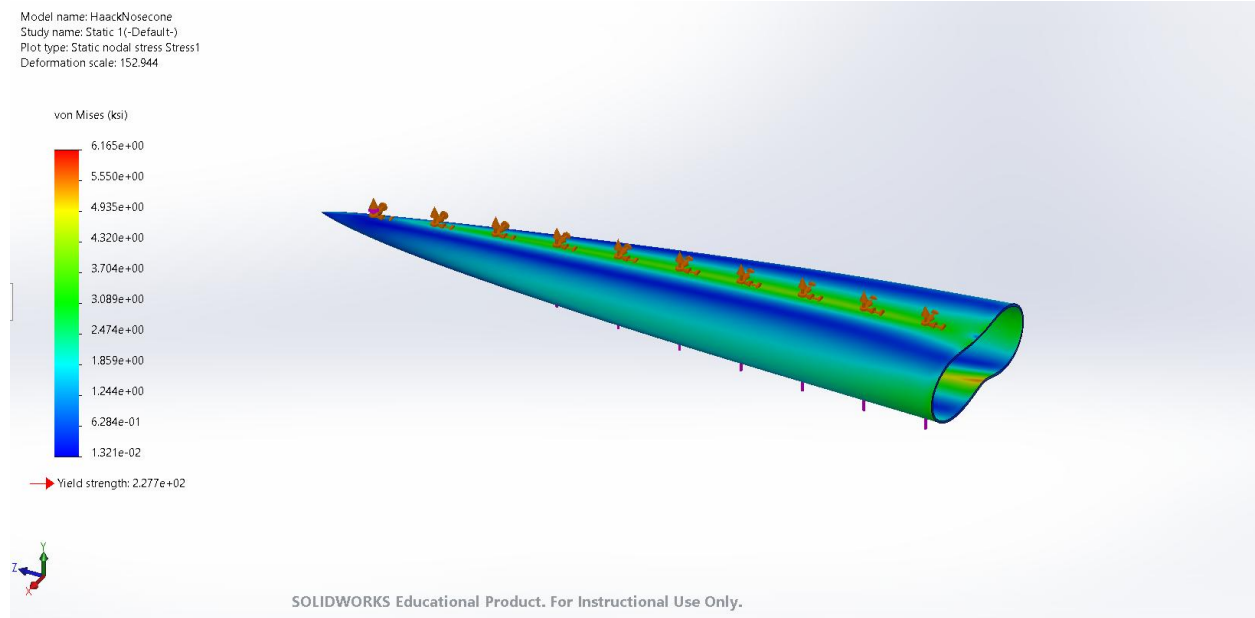


Fig. 10: Nosecone Ground Impact Simulation

3.2 Airframe Design Process

The airframe is defined by its inner diameter, thickness, lengths, and material. Regarding the inner diameter of the rocket, there is a clear lower bound set by the constraint C.1 regarding the payload CubeSat dimensions in conjunction with requirement R.2. In order to fit the hypotenuse of the 10cm-by-10cm CubeSat form factor, the inner diameter of the airframe would have to be at least 5.57in. Currently, our team does not have the capability to manufacture custom airframes, so we are limited to options that are commercially available. A simple analysis on OpenRocket was

conducted to demonstrate that when everything else is held constant, increasing the airframe inner diameter decreases the maximum apogee due to the additional weight and the larger drag forces that are induced by the wider airframe. To maximize the possible apogee of a given configuration, the drag on the airframe, therefore the inner diameter of the airframe should be minimized. However, because commercially available airframes come in discrete sizes, the team selected the smallest commercially available size of 6" inner diameter.

The next variable the team considered is the thickness of the airframe. Given constraint C.4 and the team's inability to manufacture our own airframe, there were not many options available for airframe thicknesses. Ultimately, the team chose a 0.072" thickness for carbon fiber and a 0.170" thickness for G12 fiberglass because they were the most commercially available. As will be discussed below, our simulations also verified this thickness, and the airframe should not fail. There were no other thicker, stronger options that were in stock at the deadline scheduled to purchase an airframe.

For rockets of this level, the viable material options are G12 fiberglass and carbon fiber. To investigate which would be the better option, our team employed Finite Element Analysis (FEA) to compare the performance of fiberglass and carbon fiber airframes. To do this, four main load cases were investigated. The first load case is the pressure from the black powder charges during a separation event. The airframe would need to withstand an internal pressure of 5.3 psi without failing. Secondly, the airframe must withstand a compressive force equal to the maximum upward thrust exerted by the M1845NT-P motor. Thirdly, the airframe must not rupture upon hitting the ground during landing. Finally, the airframe must be able to withstand zippering caused by the shear force applied to its lip during the recovery process. These simulations were conducted using the SolidWorks Simulation tool. The results are presented below.

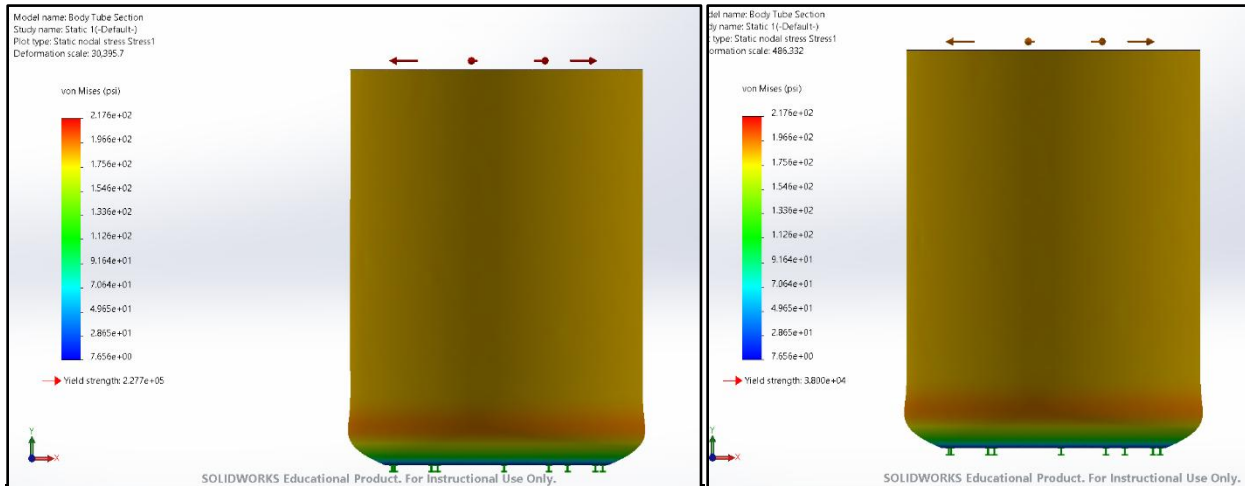


Fig. 11: Carbon Fiber (Left) and G10 Fiberglass (Right) Von Mises Stress from Black Powder Separation

The simulation results shown in Fig. 6 models the load case of pressure exerted from the black powder charges. It shows that the resulting stresses are not above the yield strength of either material. In fact, the factor of safety of the carbon fiber and G10 fiberglass are 1046 and 174.6, respectively. Additionally, the black powder charges are designed to break the shear pins, which will fail at a pressure of about 5.2 psi, so this simulation represents the worst case. It would be expected to observe that the stresses resulting from the black powder charges are below what was simulated here.

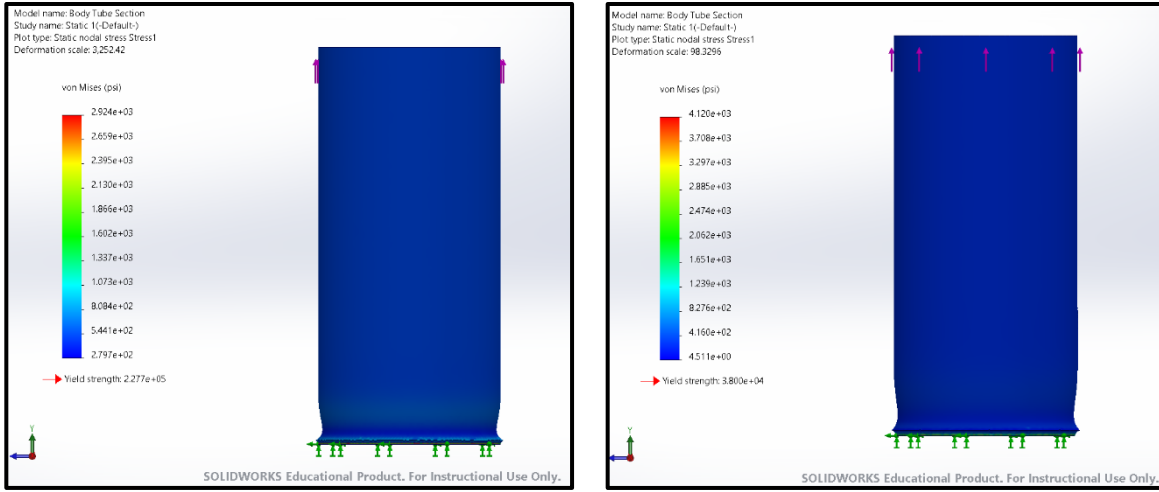


Fig. 12: Carbon Fiber (Left) and G10 Fiberglass (Right) maximum tensile stress

This load case represents the maximum possible tensile that the body tube can experience. It represents the full mass of the rocket undergoing the maximum acceleration predicted by OpenRocket. As Fig. 10 shows, the carbon fiber experiences a maximum stress of 1292 psi and the fiberglass experiences a maximum stress of 4120 psi under such a load. The carbon fiber and G10 fiberglass have respective FOSs of 77.8 and 9.2.

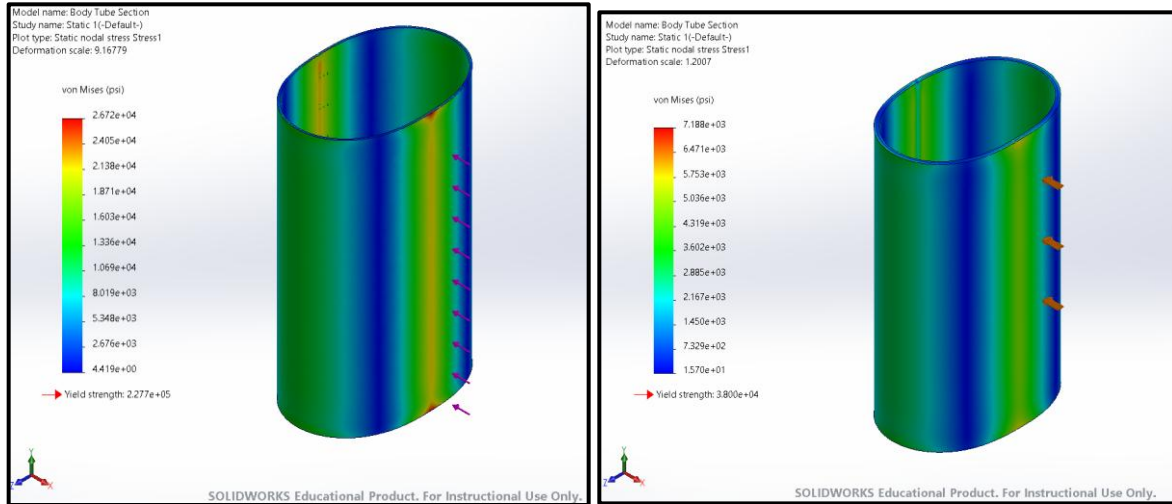


Fig. 13: Carbon Fiber (Left) and G10 Fiberglass (Right) Ground Impact Simulation

Figure 11 shows the results of a ground impact test conducted on a section of the airframe. Using the same equations, (1), (2), and (3), the worst case ground impact force was calculated to be around 369 lbf. The carbon fiber airframe experienced a maximum stress of 25720 psi and still held with a factor of safety of 8.52. The fiberglass airframe section failed this load case so catastrophically that the deformation of the mesh caused the simulation to diverge and so the full load case could not be solved. The fiberglass simulation shown represents a load case of only 28%, or about 103 lbf, and it still almost fails. This led the team to the choose carbon fiber for our body tube material.

In addition, to the simulations supporting the carbon fiber over the fiberglass, the metric of material weight must be considered. In rocketry applications, weight is a major factor in deciding components. From literature review, G12 is a denser material that is not as strong as carbon fiber and is only available in a larger thickness. The main drawback of carbon fiber is its associated cost. However, our team's budget allowed for the more expensive purchase, so carbon fiber was selected to be the airframe material.

3.3 Fin Design and Material Model Process

The fins, the most customizable aspect of the aero-structures subsystem, represent a unique opportunity in a COTS category to showcase a thorough engineering optimization process. Herein, our team will describe the optimization process that was developed to guide the design of the fin geometry for Trinity. The fin variables that we consider are the number of fins, the fin cant, the chord lengths, the fin height, the fin thickness, and the material. The fin thickness and material are the two variables that are most related to the structural strength of the fin, so the team began by deciding what these would need to be. Based on commercially available parts, the team needed to decide between carbon fiber fins at 3/16" thickness or G12 fiberglass at 1/4" thickness. Ideally, the team would select the thinnest fins that are able to withstand the loading cases. The team used FEA to differentiate between these options. The first load case is pressure applied to the fin tips which is simplified to a simulation setup where everything was fixed in place except one fin and a load was applied to the top edge of the fin. The loading condition applied represents a 300lb force spread between the two fins, a worst-case landing scenario.

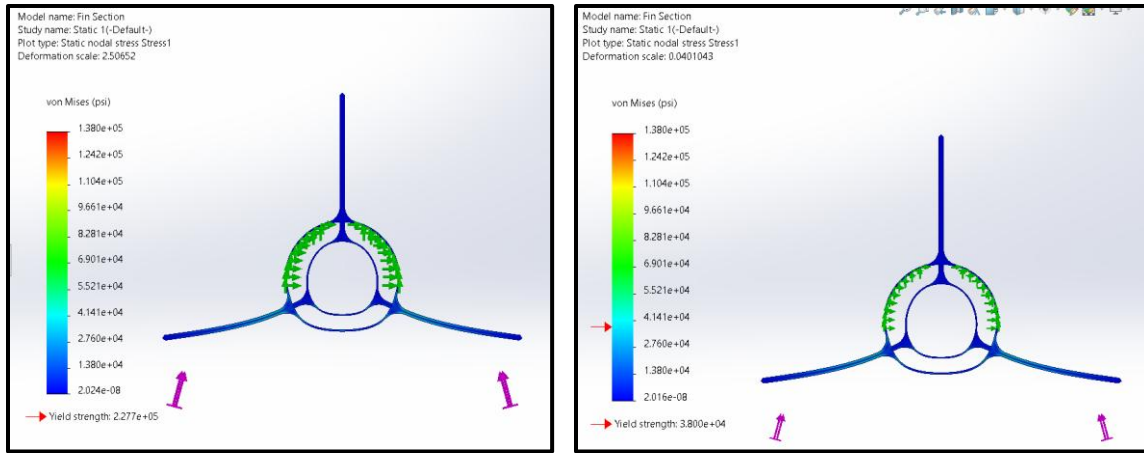


Fig. 14: Carbon Fiber (Left) and Fiberglass (Right) Fin loading

In Fig. 12, the stresses in the fins are shown. For the carbon fiber fins at 3/16", the factor of safety is 2, while the factor of safety for the fiberglass fins at 1/4" thickness is 0.28. Based on the loading conditions and resulting factors of safety, the fiberglass fins would not be able to withstand the maximum possible loading case, leaving carbon fiber as the safest choice. The downside of carbon fiber is the additional cost, but it is a lighter material that has stronger mechanical properties. The team decided to choose the carbon fiber fins because of its reduced weight and additional strength benefits while remaining within our team's budget.

To help validate the fin failure simulations above, the team worked to develop a custom material model of the carbon fiber sheets that was purchased for the fin material. Particularly, the team was interested in seeing how the angle of fibers affects the properties of the carbon fiber plates and if the material could be treated as an isotropic material or not. Members of the team used a CNC water jet to cut test specimen out of the fin stock material. Specimens were cut in vertical, horizontal, and 45-degree angles (10 of each) relative to the fiber direction in the material. These specimens were then tested in a 3-point bending experimental testing setup.

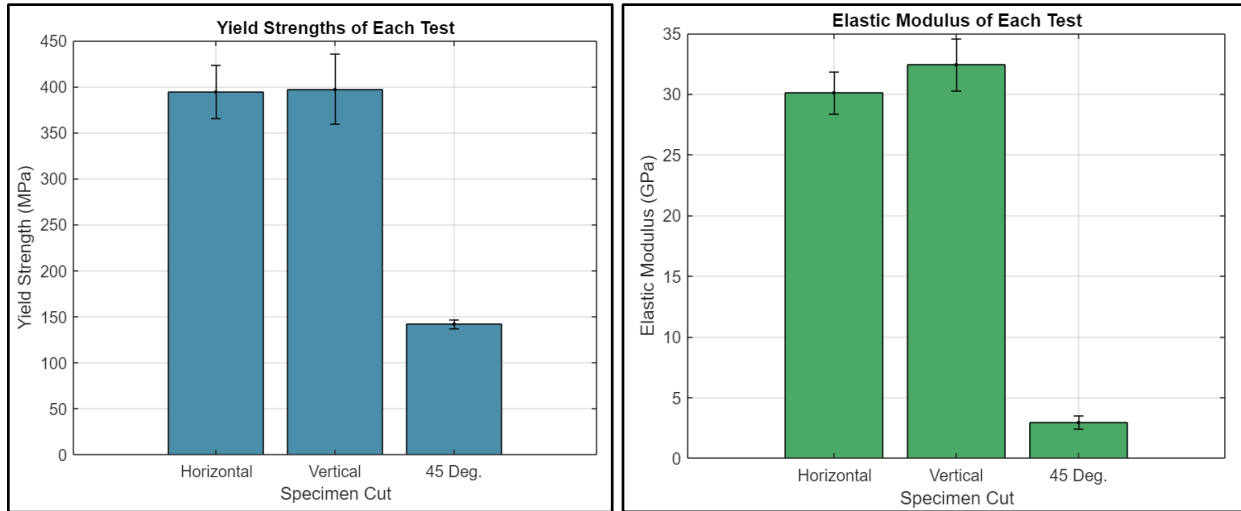


Fig. 15: Yield Strength (Left) and Elastic Modulus (Right) Results

From the results, shown in Fig. 13, it is clear that the horizontal and vertical specimen behave very differently from those cut at 45-degrees. This is a very important finding that will necessarily guide our design this year and in years to come. This demonstrates that it is very important to experimentally validate literature values so that the team's simulations are as accurate as possible. The numerical findings for the fin material's yield strength and elastic modulus are presented in the table below.

	Mean Yield Strength (MPa)	Standard Deviation (MPa)
Horizontal Cut	394.48	28.848
Vertical Cut	397.16	38.166
Angled Cut (45 deg)	141.96	5.0649
	Mean Elastic Modulus (GPa)	Standard Deviation (GPa)
Horizontal Cut	30.118	1.746
Vertical Cut	32.426	2.1474
Angled Cut (45 deg)	2.9468	0.56005

Table 2: Mean and standard deviation results

The development of this material model serves to validate our simulation results to better inform the team's decisions. If this experimentation had not been conducted the team might have falsely assumed it could continue to decrease the thickness of the fin and still maintain a factor of safety above 1. However, this was using the inflated literature values that need to be lowered to match the experimental data. To include these findings in our design decisions, the team made sure to cut the fins out so that the weave direction would be in the vertical and horizontal arrangement for greater strength.

The remaining fin variables have less to do with the structural strength of the fin and more to do with the aerodynamics of the fins. The first variable to consider in this category is the number of fins. The team needed to decide between 3 or 4 fins. The resulting apogee and stability were simulated with OpenRocket across a range of fin heights to determine how the number of fins affects these response variables.

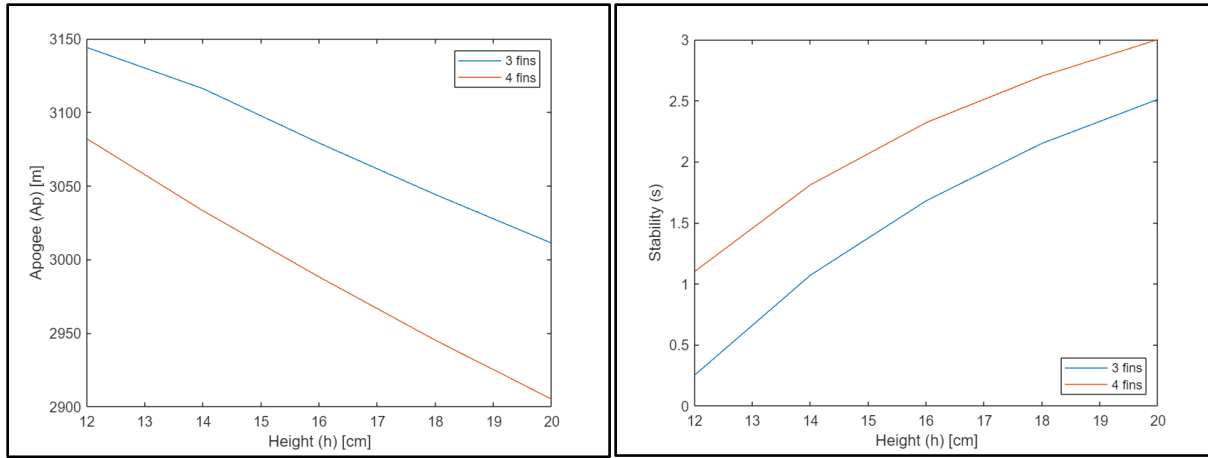


Fig. 16: Apogee (Left) and Stability (Right) Response for 3 and 4 Fins

From Fig. 14, it is clear that for every height examined, the 3-fin system has a greater apogee but smaller stability. However, it is also clear that both designs allow for the desired range of 10,000 feet (3048m) and an ideal stability around 2. Therefore, the team chose to go with a 3-fin design, cutting material costs and design complexity.

The next variables to consider are those directly related to the side profile of the fin, such as height, chord length, etc. To understand how these variables relate, the team used design the optimization feature included in OpenRocket to aid us this year in determining the optimum fin geometry. In addition, we used research conducted in years past to inform our decision. Last year, we conducted a design of experiments (DOE) to generate a large number of variable permutations to test together to infer their relationships. The fin height and chord length were the primary variables studied. The DOE consisted of these two parameters at 5 levels each. Stability and apogee were recorded for each combination. Using MATLAB and OpenRocket, the team completed the DOE and summarized the findings in the following figure.

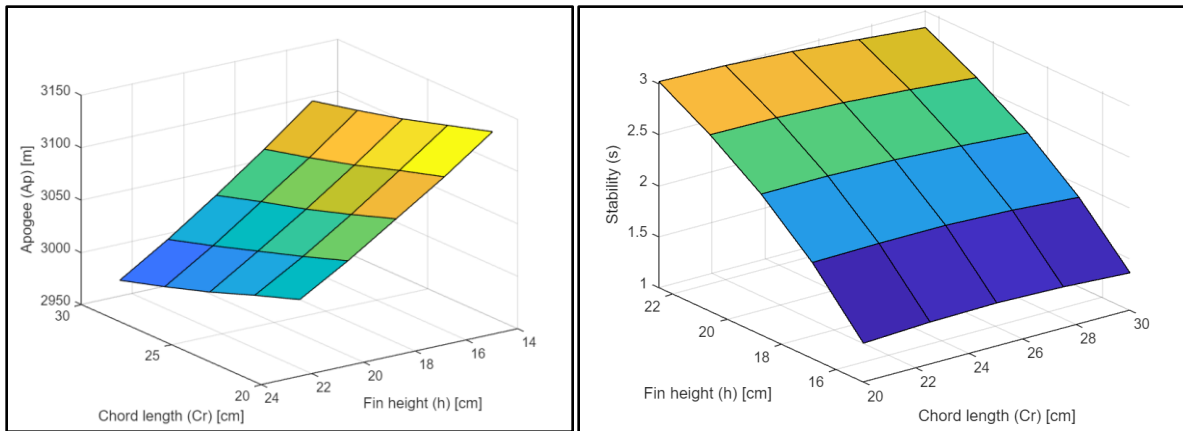


Fig. 17: Apogee (Left) and Stability (Right) Sensitivity Plot

The results provide critical insights into the relationships between the parameters and the response, allowing the team to draw meaningful conclusions about the fin design. One such conclusion was that fin height has a greater effect on the apogee and stability than the chord length does. Therefore, the team decided to use a chord length of 11.81in (30cm) for all subsequent design iterations.

Using this information, the team used the goal seek functionality in the OpenRocket Optimization tool to cause the apogee to approach 10,000 feet while maintaining acceptable stability and fin flutter margins. This optimization led to the fin design shown in figure 16.

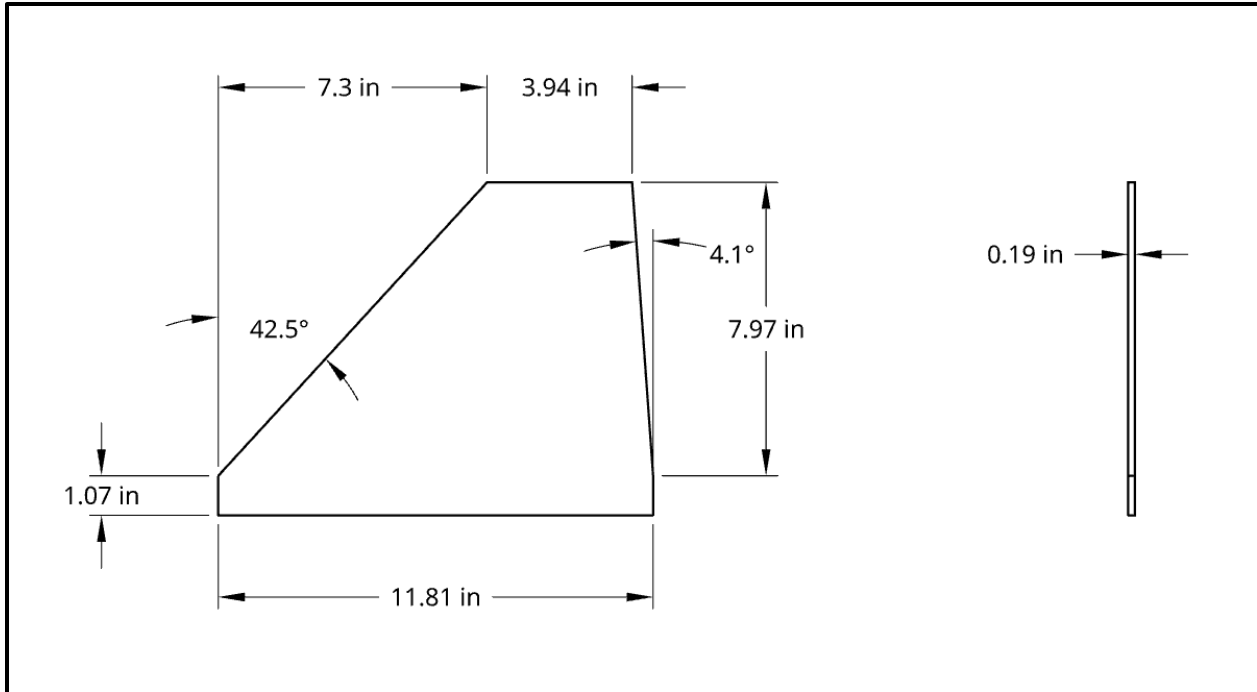


Fig. 18: Trinity Fin Design

Staying below the fin flutter velocity at all points throughout the flight is critical to maintaining a stable flight. The team calculated this function out specific fin geometry using MATLAB and equations found in “How to Calculate Fin Flutter Speed” by Zachary Howard, an article in the July 2011 issue of Peak of Flight magazine by Apogee Rockets [1].

$$V_f = a \sqrt{\frac{G}{1.337R^3P \left(\frac{c_t}{c_r} + 1\right)}} \quad (8)$$

$$R = \frac{h}{\frac{1}{2}(c_r + c_t)} \quad (9)$$

Where V_f is the minimum velocity to cause fin flutter, a is the speed of sound, G is the shear modulus of the fin material, R is the aspect ratio of the fin, P is the air pressure, h is the height of the fin, c_r is the root chord of the fin, c_t is the tip chord of the fin and t is the thickness of the fin. These equations yielded the following graph in figure 17 showing that our fins are in absolutely no danger of experiencing fin flutter.

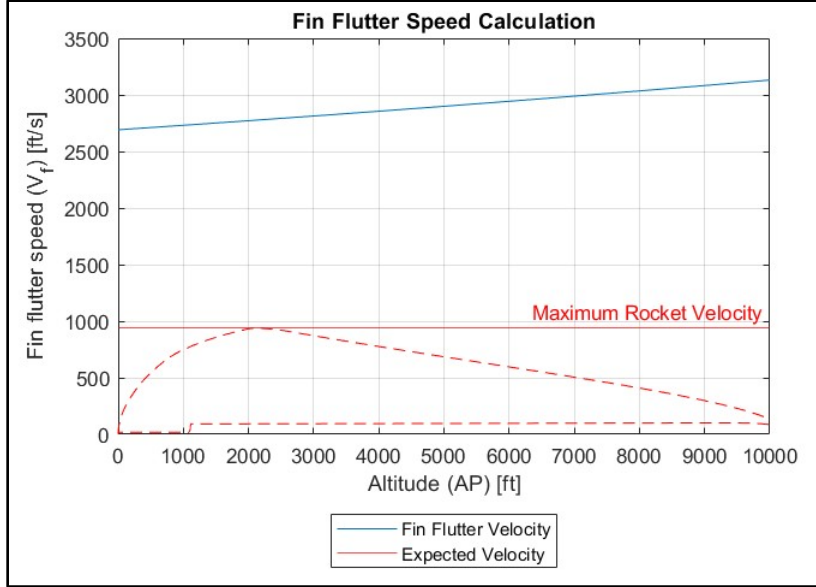


Fig. 19: Fin Flutter Speed as a Function of Height Above Ground

3.4 Boat Tail Design

This year, to develop the team's ability to manufacture components in house, we designed and created our boat tail using only raw materials for the first time. There were not many variables of the design that we could change, with the forward diameter required to be the same as the fin can's diameter, and the aft diameter required to be the diameter of the motor tube attachment ring for the same reason. This only leaves the material and the length of the boat tail as design parameters. The material of the boat tail had to be a woven tube of fibers that could be laminated in place with epoxy. This left us with the choices of Kevlar sleeving, Carbon Fiber sleeving, and fiberglass sleeving. These sleeves were quite inexpensive, so we made our decision based on the material properties of the weaves. The manufacturers reported tensile strength in all cases, so the comparison was simple. Carbon fiber was the strongest material, so that is what we chose. We validated the acceptability of this strength with a CFD simulation of the pressures that the boat tail might experience shown in Fig. 14. The length was limited by the flexibility of the carbon fiber weave. If the boat tail was too short, the weave would be forced to change diameters too quickly and would lead to poor surface quality. We were limited to the range of 3.5" to 4" of length with 4" having the most favorable stability properties.

IV. Manufacturing Process

4.1 Nosecone Construction

The nosecone itself was purchased from a vendor. A permanent 3D printed threaded ring was inserted into the nosecone to act as a retainer for the GPS system. This ring was contoured to the inner form of the nosecone for a secure fit and mounted in place using aerospace-grade epoxy. The nosecone was fitted to the rocket using a coupler which was inserted into its inner surface and extended past the end of the nosecone to fit into the inner diameter of the rocket's upper airframe. Aerospace-grade epoxy was used to the coupler to the nosecone. Holes were drilled in the nosecone coupler and threaded brass inserts were attached to 3D printed plates located behind the holes so the coupler could be securely fastened to the airframe using screws. Next, the GPS module was installed in the nosecone. This GPS module was 3D printed and designed to mount the GPS and screw into the permanent ring that was installed in the nosecone. This allows the module to be taken out of the nosecone and activated before placing it back in the nosecone for launch. The GPS module also includes a GoPro camera, so a hole was drilled in the coupler to allow the camera to see out. An acrylic film was mounted as a window to reduce drag. To finish the nosecone, an automotive body wrap was applied to the outside to be able to customize the aesthetics and ensure a very smooth finish

4.2 Forward Airframe

The forward section tubing had to be cut from a 60" length. A band saw was used to cut the forward section to its desired length of 33.5". Additionally, two camera holes were cut using a drill press to allow both a nosecone GoPro and an Electronics bay GoPro camera to have visibility out. Next, four screw holes were drilled to match the screw holes in the nosecone coupler to secure the two parts together. On the opposite end of the forward airframe, six shear pin holes were drilled and threaded to allow shear pins to be mounted and hold the main parachute compartment closed until needed. A permanent bulkhead is installed in this forward airframe section that serves to be the link to the main parachute tether. Aeropoxy mixed with fiberglass filler was placed on the edge of either side of the bulkhead to secure it to the airframe. Next, pressure holes were drilled in the forward section of the airframe to allow for pressure changes with the GPS and nosecone when in flight. Finally, the airframe was wrapped in vinyl to create a smooth surface and custom aesthetics.

4.3 Electronics Bay Housing Construction

The electronics bay housing consists of a 1" switch band section around a 13" coupler. The internal components are held between two bulkheads on either end of the coupler. The bulkheads are held in place by a lip that fits into the edge of the coupler section and held in tension by threaded metal rods that also secure the inner electronics bay sled in place. The 1" section also had to be cut on the band saw, and was then mounted to the coupler, providing a stop in the middle for the forward and aft sections. A camera hole was also cut in the coupler to align with the hole cut in the forward airframe, allowing the GoPro camera to see out. A piece of polycarbonate was mounted to the inside of the coupler tube, covering the hole to protect the camera and prevent airflow. Additionally, three holes were cut in the switch band section, aligning with screw switches on the electronics board so the black powder charges can be activated only once the rocket is on the launch rail. Shear pin holes were also drilled on either side of the electronics bay to accommodate the necessary shear pins, six on the forward coupler section and four on the aft coupler section. After these steps, the 1" section of the E-Bay was coated in vinyl to match the exterior of the rest of the rocket.

4.4 Aft Airframe

The aft section tubing also had to be cut to its desired length of 40". This section had four shear pin holes drilled and threaded to allow for a secure hold until the black powder separation event shears the pins. Next, pressure holes were drilled in the airframe to allow the payload section to remain in pressure equilibrium during flight. Then a hole was drilled for the rail button to be attached, which was screwed into a retaining plate and epoxied in place. A bulkhead was installed to this aft airframe section to separate the motor from the payload section of the rocket and to act as an anchor point for the drogue parachute. This bulkhead was secured in place using Aeropoxy and fiberglass filler similar to the other permanent bulkhead. Next, a coupler section was fitted to the aft end of the airframe to mount the fin can onto. The coupler was permanently mounted to the aft airframe with Aeropoxy. A retaining ring was printed out of PETG and also mounted with Aeropoxy. Threaded brass inserts were fitted into the ring to allow screws to securely mount the fin can to the aft airframe. Finally, the aft airframe was coated in a vinyl body wrap.

4.5 Fin Can

This season we implemented a fin can to allow for the ability to interchange or reuse fins as needed. First, we cut a 20" section of carbon fiber tube, and drilled holes in the forward section to align with the aft airframe. We also drilled holes on the aft side of the fin can to allow for the attachment of a boat tail, which we are implementing to reduce drag induced by the wake of the rocket. Additionally, we cut three fins slots to fit our fins. These were made of 0.1875in thick Dragon Plate carbon fiber plates which were cut to shape using a CNC waterjet according to the engineering drawings included in the appendix. A router was then used to chamfer the leading and trailing edges at 45 degrees to make the fins more aerodynamic. The motor tube was epoxied into the fin can using Aeropoxy and the fins were inserted into the slots and epoxied in place using Aeropoxy mixed with chopped carbon. We applied a fillet on the edge where the fin met the exterior airframe as well as where the fin met the motor tube. Fig. 19 shows an image of our setup. In order to keep the exterior fillets smooth to reduce sanding, we used a PVC pipe which does not bond to the epoxy. Then, after the epoxy had cured, the fillets were inspected and sanded as necessary to ensure the correct shape, then another thin layer of dyed epoxy was added to bring back the smooth finish. Then, the boat tail, which is discussed in section 4.6, was added to the end of the fin can. Finally, the fin can was applied with a vinyl body wrap.¹



Fig. 20 Fin Construction Setup

4.6 Boat Tail

The boat tail is a new project that we took on this year in order to continue to develop our team's ability to develop and master new manufacturing techniques and increase the amount of in-house manufacturing to cut costs. We printed a boat tail negative out of ABS and used laminating epoxy to lay up several layers of tubular carbon fiber woven sleeving on top of it. This we cured in a custom designed and fabricated epoxy oven. After the carbon fiber laminate had cured in the oven, we removed it and cut away and sanded the excess material, leaving just the carbon fiber and its mounting piece. We secured the custom boat tail piece to its mount with JB Weld, and then attached the boat tail mount to the aft of the fin can using brass threaded inserts for a secure hold.

4.7 Full Rocket CFD

To better understand the forces on the entire rocket, a CFD simulation was created using ANSYS. Taking the full CAD model, editing to be watertight, and then inserting into the watertight geometry workflow inside of Fluent Meshing, the rocket was meshed and then inserted into solution mode. To reduce computational time, the rocket was divided radially into thirds along its long axis. This reduces cell count and therefore computation time significantly, allowing for a quicker iterative process. The full volume mesh is seen in Figure 21. Once the mesh is divided and ready to be solved, the boundary conditions and convergence requirements are input. A no-slip boundary condition was applied to the body of the rocket. The inlet boundary was set to be Mach 0.5 and a symmetry condition was set on the division walls of the mesh.

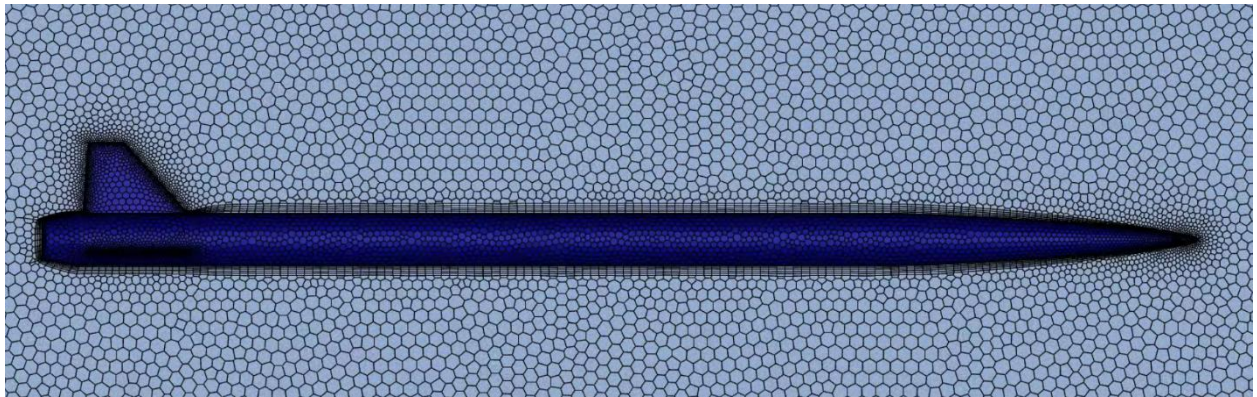


Fig. 21 Volume Mesh of the Entire Rocket

Once the simulation has finished running, a contour plot was made for velocity and then a plot of the streamlines was made. These are seen in Figure 22 and Figure 23.



Fig. 12 Velocity Contour Plot

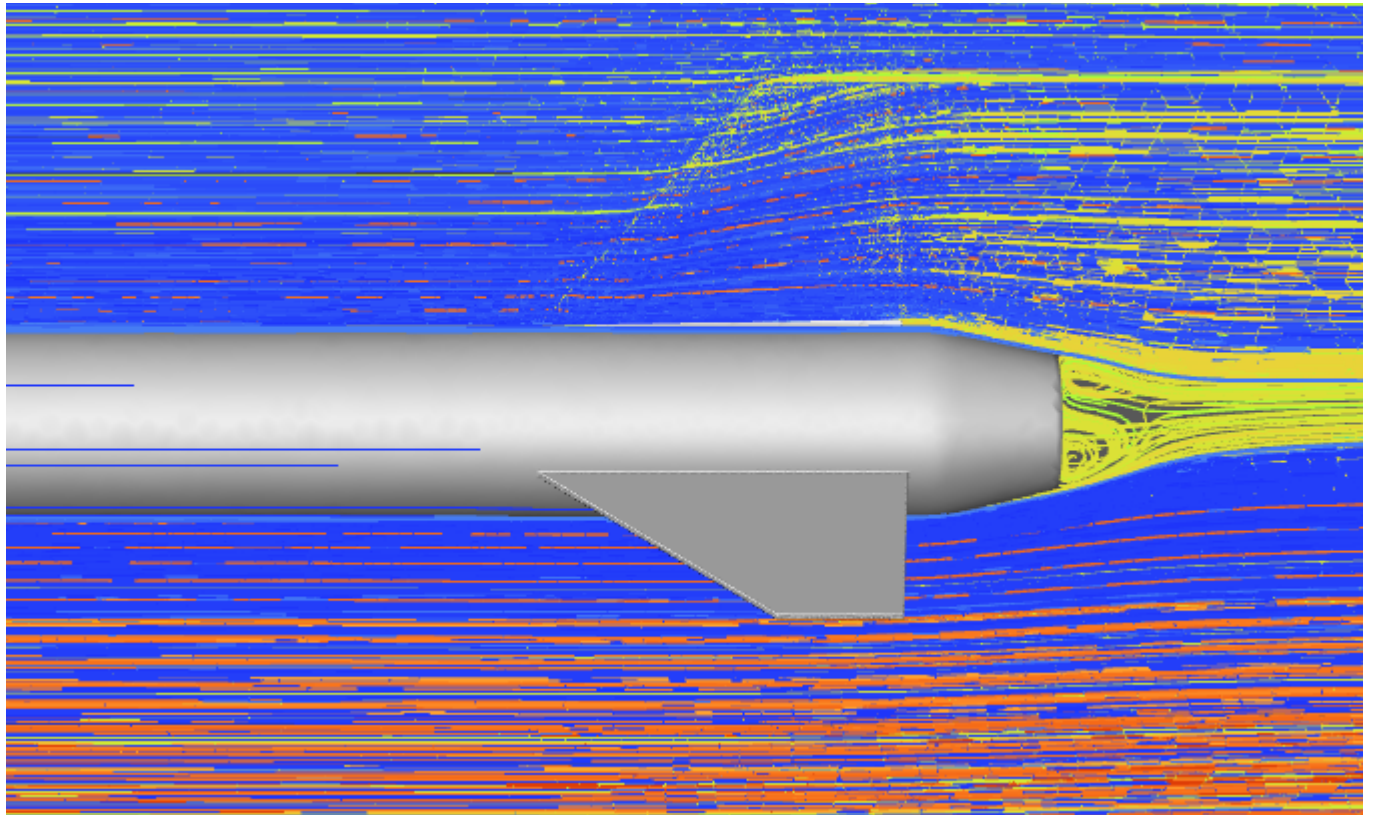


Fig. 22 A Plot of the Streamlines

The CFD simulations give us good contour plots to help visualize the flow of the air around the rocket. However, they also give us data on the drag forces experienced by the rocket. Additionally, the drag force can then be used to calculate the drag coefficient, a very valuable number when it comes to rocket design as it indicates aerodynamic efficiency across geometries. Since the simulation is over the entire rocket, the boundary for the air is also large. This causes a large area to split into cells and can create issues when it comes to optimizing cell count. The team is continuing to work on cell size optimization. Table 3 shows the different drag coefficients and drag forces at Mach 0.5 with different cell counts.

Cell Count	Mach Number	Drag Coefficient	Simulated (1/3) Drag Force [N]	Drag Force [N]
665,691	0.5	0.42397	47.309	141.93
666,260	0.5	0.42386	47.295	141.89
673,187	0.5	0.42350	47.250	141.75
1,410,633	0.5	0.39258	43.805	131.41
1,433,399	0.5	0.39326	43.881	131.64

Table 3: Drag Properties at Varying Mesh Sizes

Overall, the CFD simulation gave students experience in learning how to do aerodynamic simulations and how they can be applied to our apogee estimations. In the future, this simulation will be run at Mach values from 0.01 to 0.82 to obtain the drag forces at differing velocities. This will allow the team to produce drag curves for the rocket to better refine our apogee simulations.

Recovery Subsystems

I. Recovery Overview

The recovery subsystem follows a conventional dual deployment, dual separation system. There are two parachutes in this system, a 96 in toroidal main parachute and a 24 in elliptical drogue parachute. Each parachute is attached via a simple system of Kevlar tethers and quick links. This system allows for accurate ground testing and easy repeatability between loading and unloading the system into the rocket. The drogue parachute will be deployed at apogee, (approximately 10,000 ft), and the main will be released at around 1,200 feet. It is important to note that the main parachute deployment can vary slightly depending on wind/air conditions. Higher wind speeds force our team to consider lowering the release altitude to around 1,100 ft, while slower windspeeds will allow us to remain at 1,200 ft. This height allows our main parachute plenty of room to open fully, while minimizing the potential lateral drifting distance. OpenRocket predicts our lateral drifting distance to be approximately 500 ft when accounting for a 12-mph wind speed. The parachutes are deployed by barometric RRC3 Sport Missleworks altimeters, which are powered by standard industry 9V batteries. Trinity utilizes two of these altimeters, with separate power sources and separate wiring for redundancy purposes. Separation is accomplished via FFFFg black powder charges. The drogue bay will have a charge size of 2 g, with a 2.5 g redundancy charge, and the main bay will have a 3 g charge with a 3.5 g redundancy charge. These charge sizes were thoroughly ground tested to ensure complete separation occurred at these chosen sizes. Figure 23 shows an overview of the recovery system.

If the opening shock impulse is too high and the shock cords are too thin, a body tube failure known as “zippering” will occur. Zippering is the shearing of the body tube in the axial direction. This shearing is the result of tension in the tethers once the parachute is deployed and catches air, causing compression against the airframe. In order to prevent this failure, a foam cushion, known as a “fireball”, can be placed over the region of the shock cord that passes over the edge of the body tube. The fireball distributes the shearing force over a larger area, decreasing stress on a given unit area of the airframe. The Trinity recovery design will incorporate such a cushion on the shock lines for both the main and the drogue chute. Each fireball is wrapped in a Kevlar sheath that will protect it from the black powder charges. Additionally, to prevent damage to our main parachute and corresponding subsystem components, Trinity’s recovery system will utilize a reefing ring to lower the initial shock force transferred to the rocket during the sharp transition from freefall to drogue fall speed. The reefing ring is placed along the main parachute lines, about 2/3 from the bottom, which helps control the rate at which the parachute opens, reducing the initial shock, which as a result helps to prevent potential damage to the system.

The bulkheads comprising the internal anchor for the recovery system are $\frac{1}{4}$ ” thick G10 fiberglass. To validate the use of such thin, lightweight structures, simulations were run in SolidWorks. A detailed analysis of the bulkheads will be placed in the Recovery System Testing Appendix.

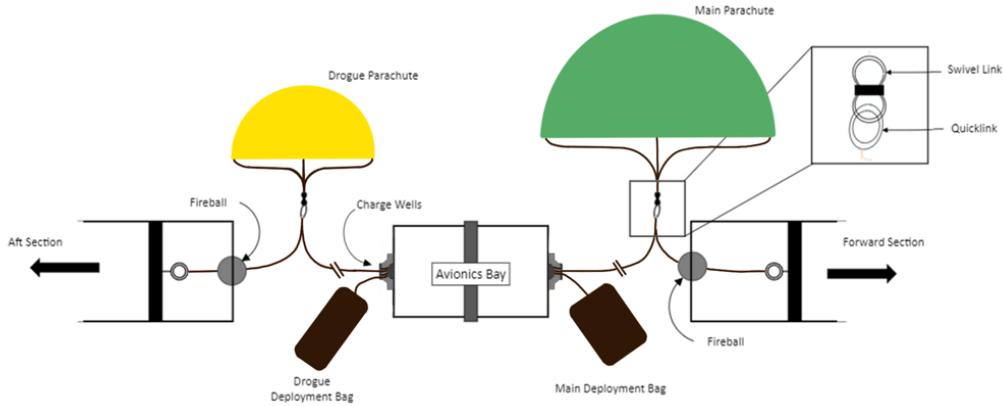


Fig. 23: Recovery System Overview

II. Recovery Design Process

The design for recovery follows a linear step-by-step process. Due to the competition's requirement of COTS components, the system is restricted in customizability of components. Instead, the recovery subsystem can customize the layout of their system. The process detailed below provides a guide to each design decision and insights into the assumptions made.

2.1 Parachute Selection

Many considerations and calculations were considered in the choosing of our main and drogue chute types and sizes. Following standard guidelines for a rocket this size, the desired initial and final decent speeds were 90 ft/s for the drogue and 19 ft/s for the main chute for its final descent and impact speed with the ground. Knowing the descent speeds along with the atmospheric conditions, the theoretical main and drogue chute size are determined (refer to Figure 23). With these theoretical values, a standard size and style of parachute can be chosen that meets these requirements.

Calculating Parachute Size						
Variable	Description	Units	Inputs	Outputs	Equations Used	
A_m	Area of Main Chute	ft^2	-	68.40	$A_m = \frac{2mg}{\rho C_D V_{impact}} - \frac{\pi D_r^2}{4}$	
D_m	Main Chute Diameter	ft	-	9.33		
D_r	Drogue Chute Diameter	ft	-	2.00	$D_m = \sqrt{\frac{4A_m}{\pi}}$	
m	Mass of Rocket	slug	1.56	-		
g	Acceleration due to Gravity	ft/s^2	32.20	-	$D_r = \sqrt{\frac{8mg}{\pi r C_d v_d^2}}$	
π	Pi	N/A	3.14	-		
ρ	Density of Air	ft/s	0.0047	-	$D_r = \sqrt{\frac{8mg}{\pi r C_d v_d^2}}$	
C_d	Drag Coefficient	N/A	0.93	-		
V_{impact}	Desired Impact Speed	ft/s	17.98	-	$D_r = \sqrt{\frac{8mg}{\pi r C_d v_d^2}}$	
V_d	Desired Descent Speed	ft/s	86.00	-		

Drogue Parachute Decision Matrix										
Options:		Annular			Parabolic			Elliptical		
Wants Criteria	Weight Factor	Rating	Value	Weighted Score	Rating	Value	Weighted Score	Rating	Value	Weighted Score
Cost	4	7	\$80	28	8	\$56	32	7	\$80	28
Low Pack Volume	4	8	8.6 in^3	32	8	9 in^3	32	8	12 in^3	32
C_d	6	7	~1	48	7	0.97	42	9	1.5	54
Durability	7	7	Nylon	49	7	Nylon	49	7	Nylon	49
Stability	8	7	-	56	6	-	48	7	-	56

Total Score:	-	-	-	213	-	-	203	-	-	219
--------------	---	---	---	-----	---	---	-----	---	---	-----

Main Parachute Decision Matrix										
Options:		Toroidal			Elliptical			Iris		
Wants Criteria	Weight Factor	Rating	Value	Weighted Score	Rating	Value	Weighted Score	Rating	Value	Weighted Score
Cost	5	6	\$420	30	7	\$378	35	8	\$260	40
Low Pack Volume	3	6	140 in ³	18	7	121 in ³	21	7	92 in ³	21
C _d	6	7	2.2	42	8	2.7	48	7	2.2	42
Durability	7	9	Ripstop	63	8	Ripstop	56	6	Nylon	42
Weight	6	7	25 oz	42	5	30 oz	30	7	18 oz	42
Total Score:	-	-	-	195	-	-	190	-	-	187

Fig. 24: Parachute Size Calculations (T) and Decision Matrices (B)

To narrow our options further, each design decision was weighed against another using decision matrices. For our parachutes, the matrix consisted of 7 styles of parachutes: annular, toroidal, disk gap band, ringsail, elliptical, and SkyAngle. An example of the top three options is shown in the matrix above. The list consists of various criteria (durability, stability, packing volume), each multiplied by a weight factor.

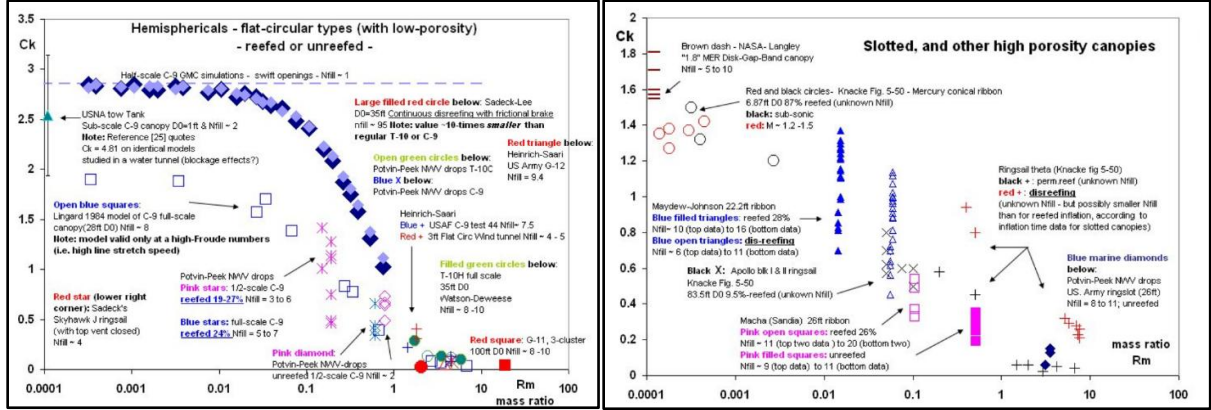
Durability is a measure of the parachute's ability to tear and was designated as the most important criteria because if the parachute breaks, every other significant element of the chute is sabotaged. Additionally, failure prevention of this category is most optimal. Since we still opted to purchase a conventional chute with drogue dimensions, the style of the drogue chute needs to maximize its durability. Certain parachutes are designed for certain requirements. For example, disk-gap band parachutes were developed for high-altitude rocket applications and planet re-entry. On the other hand, parachutes such as ringsail often serve as escape system parachutes. For our system, we need a small parachute with a high durability. The Toroidal and Skyangle chutes ranked highest for main chutes, while elliptical chutes had the highest score for drogue chutes. Following this process, it was decided that the Trinity system would utilize a 96in Toroidal Rocketman High Performance Parachute for the main and a 24in Elliptical Apogee parachute for the drogue.

2.2 Shock Forces

Based on the sizing of our parachutes, we can then investigate our shock forces. Shock forces occur due to the drag forces produced by the parachute, and therefore a sudden change in velocity when the parachute deploys and opens. This force is extremely important to consider when designing an adequate subsystem, as shock forces can easily break components if not accounted for. Our team created a shock force calculator in Excel utilizing the following equations to give us a simplistic view of the forces our rocket body may experience. The mass ratio can help determine the shock force a parachute will implement on any given system. Unfortunately, there is no simple, direct relation between these two values, instead various experiments and research were performed to help determine an approximate shock coefficient. Graphs of the various research done relating these two factors are provided below.

$$F = \frac{1}{2} C_k (C_D S)_0 \rho v^2 \quad R_m = \frac{\rho ((C_D S)_{sd})^{3/2}}{m} \quad (10)$$

This allowed our team to gain an idea of how our parachutes will affect the rest of our recovery system. If we deemed these forces too high, then we could revert to our parachute decision matrices and reevaluate our choices. It is important to note that these equations are highly simplified for our recovery system, as it assumes all the force generated from the parachute is instantaneously translated throughout the rest of the recovery system. Realistically, with correct black powder sizing and adequate testing, our recovery system should rarely experience the maximum shock force. The reason for this is because the shock force equations utilized do not factor in any drag force that may be acting on the body of the rocket. Instead, the equation treats the payload-parachute system as falling with taunt shroud lines, at the maximum possible velocity under recovery. It is evident, especially after our team's first test launch, that this is not the case regarding our system. Figure 25 shows the calculation process and results for the maximum shock force on the system.



Shock Force Calculations						
Variable	Description	Units	Inputs	Outputs (lbf)	Outputs in Newtons	Equations Used
F	Upper Limit of Snatch Force	lb.	-	550.08	2446.90	$F = \frac{1}{2} C_k (C_d S)_0 \rho v^2$
ρ	Density of Air	slug/ft ³	0.0024	-	-	
v	Velocity at Parachute Release	ft/s	87.27	2.84	-	
C_d	Drag Coefficient	N/A	2.20	-	-	
S_0	Surface Area	ft ²	68.39	-	-	
C_k	Upper Coefficient of Shock	N/A	0.40	-	-	$\frac{\rho((C_d S))_{sd})^{3/2}}{m}$
R_m	Mass Ratio	N/A	-	-	-	

Fig. 25: Relation between Shock Force and Mass Ratio (T); Shock Force Calculations (B)

The maximum shock force can be calculated based on a terminal velocity fall broken by a main chute deployment. As shown in Figure 25, the maximum shock force is expected to be 550.08 lbf. Based on these shock forces we could then decide on various recovery components such as our bulkhead, tether, and quick links.

2.3 Recovery Hardware

Based on the shock force, each component of recovery hardware was chosen. The first, and most important aspect, is that these components must be well over the predicted shock force loading. Even though the recovery subsystem should never experience a full amount of shock force at any moment, that does not mean it cannot ever happen. Therefore, the system must be designed to resist a worse-case scenario. The parachutes are connected to the rocket via $\frac{1}{2}$ inch tubular Kevlar cords, rated at 7200lbs, with both the main and drogue bays holding 40ft. The 40 ft drogue tether was chosen because of the added volume to the drogue bay itself, and to limit nosecone spinning when descending under drogue. It is generally reported that a tether length 3-4x the length of the body of the rocket is recommended, this allows the parachute time to open before the shock cords are pulled downwards from the weight of the rocket. Ground testing further supports this decision, as it was evident that the cords provided sufficient length for full removal of each parachute, while still allowing extra length for the parachutes to open before any downward forces occurred. Kevlar cords were chosen over nylon cords for their high strength, low elasticity, and fire-resistant properties. The cords have three sewn loops, with one located approximately one-third of the length from one end. This middle loop will be our parachute attachment points for both drogue and main.

Each connection point will have a $\frac{1}{4}$ inch stainless steel quick link, which are rated at \sim 1000lbs. The main and drogue parachutes are connected by stainless steel swivel links, which are rated at 1500lbs. and 1000lbs., respectively. Quick links were chosen because they serve as easy connection points for each component of our system. These components allow for rapid changes if there was an oversight in our initial design. These links will also allow for

quick removal of our entire recovery subsystem for transportation. Our tether system will be connected to the rocket via 2 5/16" forged steel eyebolts, located in the top payload and forward bulkheads, which are rated at 900lbs.

Instead of opting for traditional eyebolts or eye nuts, a custom recovery was designed by the team and professionally machined. This decision was made after considering all options and completing a decision matrix to narrow it down. This matrix is shown below in Figure 26. This hardware serves as connection points for both sets of tethers and the main deployment bag to be secured to each side of the avionics bay. This custom piece allows for efficient assembly of recovery components. Simulations were conducted on this custom hardware, and 6061 Aluminum was chosen to be the primary material of the machined part. A factor of safety of greater than 3 was obtained through these simulations, and further ground testing was conducted to ensure the strength of the yoke during drogue and main deployment. Further research and analysis is explained in the Recovery System Testing Appendix.

Primary Recovery Hardware Decision Matrix										
Options:		Forged Steep Eyebolt 1/4 in			3/8" U bolt Galvanized			Custom Designed Tether Bar		
Wants Criteria	Weight Factor	Rating	Value	Weighted Score	Rating	Value	Weighted Score	Rating	Value	Weighted Score
Cost	4	6	\$3.00	24	5	\$25	20	5	~\$40	20
Weight	5	7	25g	35	5	120g	25	6	90g	30
Working Load	8	6	500 lb.	48	8	1400 lb.	64	8	1500 lb.	64
Total Score:	-	-	-	107	-	-	109	-	-	114

Fig. 26: Primary Recovery Hardware Decision Matrix

2.4 Shear Pins and Black Powder Sizing

As the rocket is coasting, the fins will provide a higher drag than the nosecone, thus the rocket has potential risk of separation. To prevent this, small screws, typically made of nylon, are pushed into the sections of the airframe where separation due to recovery will occur. These screws provide just enough force to hold the rocket and prevent premature separation but will shear when the black powder charges are ignited. These small screws are called shear pins. Finding the correct shear pin size and amount is a thorough process.

When the drogue shear pins are sheared during drogue deployment, it is crucial for the main bay shear pins not to shear and separate. Thorough testing and calculations were made to ensure that premature separation of these main bay shear pins would not occur during the deployment of the drogue parachute. This impulse and momentum during deployment can be calculated easily by first obtaining mass values for the forward section that holds the main bay and its recovery components. Then an approximate fall velocity can be calculated and divided by a time in which the force acts over. This impulse time was assumed, as it is extremely difficult to determine an exact time without proper equipment. However, given the opportunity, future testing would like to be conducted to allow for more accurate results. Our team instead utilized drop testing to help us determine if our initial assumptions were accurate. Calculations conducted after this test confirmed that the six 4-40 shear pins for the main bay were adequate to withstand the force that would be exerted during drogue deployment. Calculations confirmed that the shear pins would not shear under 448.57 lbf, which results in a factor of safety of 1.67 due to the max force exerted by the upper section being 268.89 lbf. Further explanation of these calculations is included in the Recovery System Testing Appendix.

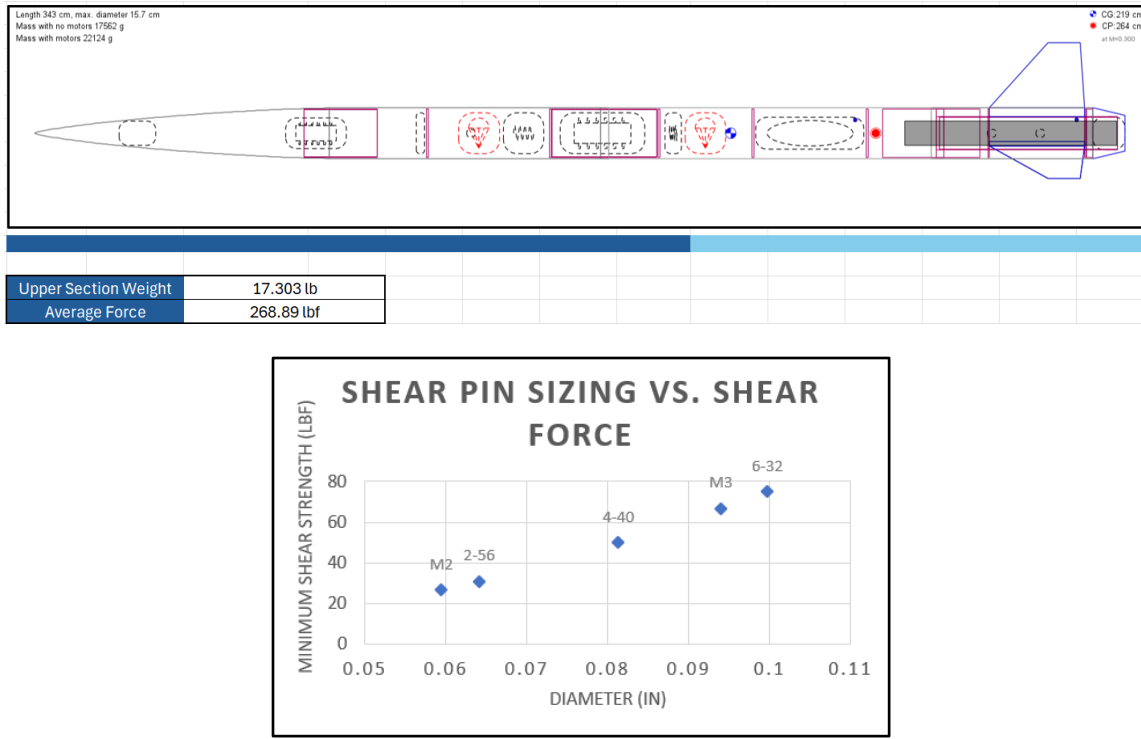


Fig. 27: Excel Document with Upper Section Weights (T); Shear Pin sizing graph (B)

Under drogue, the upper section of the rocket was estimated to produce a force of 268.89 lb. Based on these two values, a shear pin design can be chosen. The design must be readily available in the market and have a proven design that has worked before. Due to our familiarity with 4-40 shear pins, the team chose to utilize this size for both the drogue and main bays. With a minimum shear strength of 49.84lbf, the main bay would need 6 shear pins. 4-40 shear pins provide a median value between both shear force and diameter, when compared to other readily available options, this sizing is the closest to our needed minimum shear strength without maximizing the overall diameter of the screw. Therefore, six 4-40 shear pins were chosen for the main bay.

The drogue bay did not need nearly as many screws, as the only force this section may experience is a drag separation force. Two 4-40 shear pins would be the minimum for this section, however, as an added layer of safety due to potential oversights, this sizing was upgraded to four 4-40.

Decoupling Charge Size					
Main Parachute Inputs		Calculations		Final Values	
Diameter	6 in.	Pressure	5.305 psi	Grams needed	0.98 g
Length	12.6 in.	Gram Conversion	454		
Bulkhead Force	150 lbs.	BP Burn	879662		
Volume	356.2 in ³	Conversion Grams to lbs.	0.002204		

Fig. 28: Main Decoupling Charge Size Calculations

Calculations based on the internal volume of our parachute bays alongside our shear pin sizing yielded charge sizing of approximately 2g for the drogue and 3g for the main. Each parachute bay will have two charges wells; with the redundant charge at least half a gram higher than our primary charges to guarantee deployment if our first charges were to fail. Ground testing was performed with both primary and redundant charges and each test provided adequate results.

III. Recovery Manufacturing Process

3.1 Bulkheads

The five bulkheads in our system were cut out of $\frac{1}{4}$ " G10 fiberglass sheets. This was conducted using a water jet cutter that followed the design of each SolidWorks model. To ensure the holes of each bulkhead were aligned properly, a SolidWorks model of the bulkhead, along with each drill hole, was created. Then a top view was printed out and taped to the top of the bulkhead. Each edge was carefully checked to ensure everything was correctly aligned. Then each hole was drilled out using a drill press. The avionics and payload bay rods had $\frac{1}{4}$ " diameter holes, the charge wells had $\frac{1}{64}$ ", and the eyebolts had $\frac{5}{16}$ " holes. Aeropoxy with chopped fiberglass was used to epoxy our bulkheads into the airframe. The edges of the bulkhead and sides of the airframe were sanded to ensure the epoxy would adhere to all components. The forward most bulkhead, which is represented as bulkhead number one in Figure 22 below, was epoxied within the airframe on one side only. This was due to the nosecone coupler pushing up against the other side of the bulkhead. The epoxy helped secure the bulkhead against the forces of the recovery subsystem, so we felt this was an adequate exception to only epoxy one side. A small section of coupler tube was placed along the non-epoxied side of the bulkhead, which not only secured the bulkhead in the airframe when force was applied to it but also ensured that the bulkhead was perfectly perpendicular along the airframe. The bottom payload bulkhead was epoxied in as well, following the same procedures as the forward most bulkhead discussed before, however both sides were epoxied.

The five bulkheads used in the rocket were each designed differently. The two avionics bulkheads were each designed to include two rods that would hold the avionics sled. These also included two charge wells each, one to hold the primary back powder charge, and the other to hold the redundant charge. This setup was identical on both avionics-connecting bulkheads. In addition, the bulkheads housed terminal blocks on top. One bulkhead would then be used to deploy the drogue, while the other would be used to deploy the main parachute with the e-matches loaded in the terminal blocks. To secure the rods to the two bulkheads, two custom designed aluminum bars were placed on both ends. These bars, or recovery yokes, would then be used to secure tethers for the recovery system. The forward most bulkhead includes an eyebolt in the center that would be used for the recovery system as well.

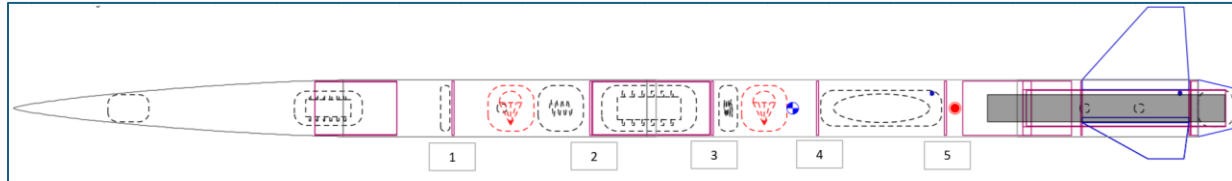


Fig. 29: Bulkhead Locations

Bulkheads two and three were held in a four-jaw chuck. The outer edge was turned such that a lip exists on the outer edge to keep the bulkheads concentric with the coupler that houses the electronics bay. The results of this process are shown in the following figure.

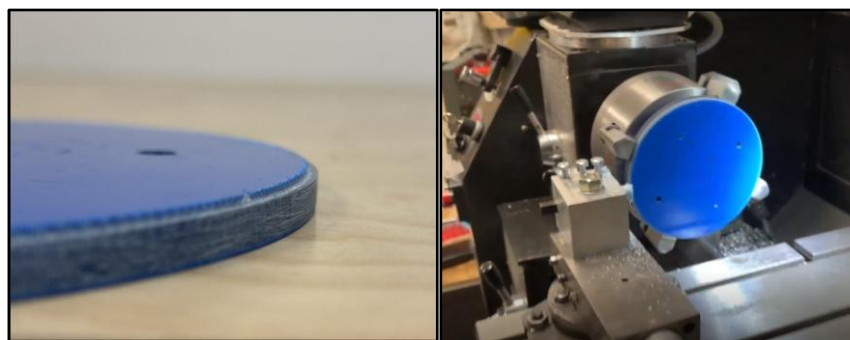


Fig. 30: Avionics Bulkhead Lip Process

IV. Recovery Electronics

Both parachutes are deployed using dual deployment capable COTS altimeters. We utilize two Missileworks RRC3 Sport barometric altimeters, one as the primary altimeter and one as the redundant altimeter. Both are powered by independent 9V batteries, which are replaced before each flight and the voltage is tested as well. In battery drain tests, each altimeter lasted for over 8 hours. The wiring schematic is shown below:

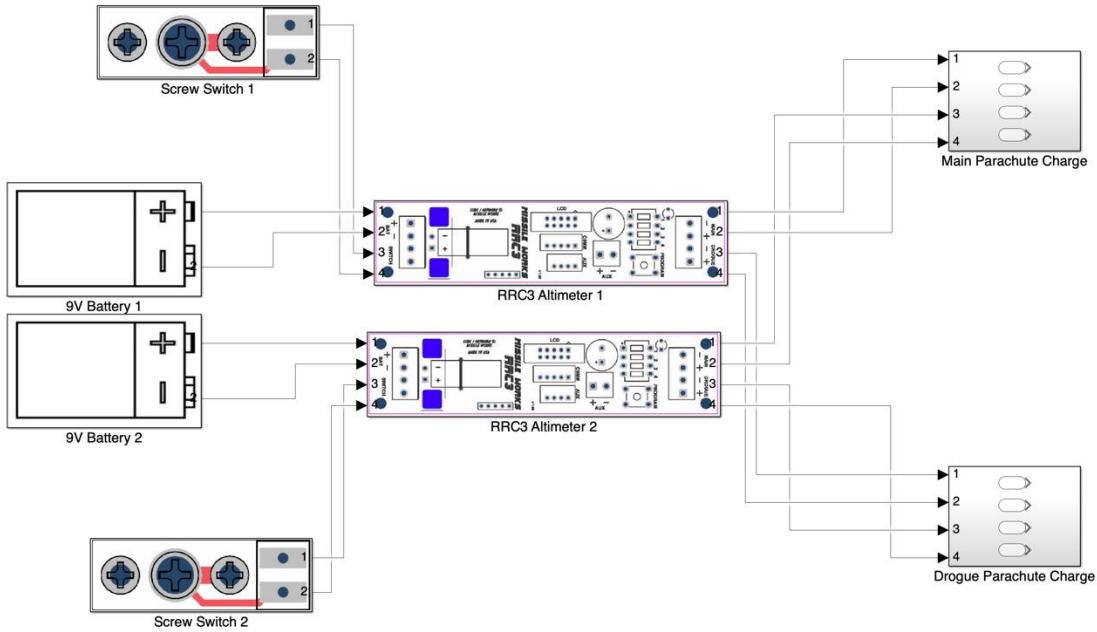


Fig. 31: Recovery Wiring Diagram

The GPS chosen was the Featherweight GPS, which communicates from the tracker unit in the nosecone of the rocket to a ground station unit over the 915 MHz LoRa band. It has performed exceptionally in all launches the team has completed over the last 3 years. It is powered by a manufacturer provided 400 mAh LiPo battery which provides 4-6 hours of operation. The GPS has a ground station unit which is connected via Bluetooth to a phone application with an integrated map, and it provides data via USB to our ground station computer simultaneously.

Avionics Subsystems

I. Manufacturing

The manufacturing complexity of many non-structural aspects of the rocket leant themselves towards 3D printing as the best manufacturing method. Below shows the decision matrix for the filaments used on the rocket, with data gathered from an independent researcher [2].

Filament	Tensile Strength (kg)	Layer Adhesion (kg)	IZOD Impact Test (kJ/m ²)	Heat Deformation Temp (°C)	Ease of Printing	Cost (per kg)	Total Score
CF Nylon	108.65	42.85	12.1	190	Medium	\$180	20
	5	5	3	5	2	0	
GF Nylon	106.95	15.65	7.5	200	Medium/Hard	\$60	14
	5	2	1	5	1	1	
ABS	63.7	36.95	22.8	83	Medium/Hard	\$30	17
	3	3	4	4	1	2	

PETG	67.4	32.6	3.8	64	Easy/Medium	\$20	14
	3	3	0	2	3	3	
PLA	82.85	45	27.4	52	Easy	\$15	22
	4	5	5	0	4	4	

Table 4: Filament Comparison

Highlighted items can be dealbreakers, depending on the model geometry and part usage. We chose to print the nosecone e-bay in CF nylon due to its superior layer adhesion compared to alternatives (since the thread strength is primarily related to layer adhesion). CF nylon was also used for the fin can attachments. ABS was chosen for the boat tail for its low cost and relatively high strength and temperature resistance which were calculated to be more than sufficient for the task. Glass fiber (GF) nylon was chosen for the primary e-bay due to its incredibly high temperature resistance. PETG was utilized for all other critical parts, including the payload holder, the payload itself, and much of the ground station computer. Crucially, PLA is used for no structural or load-bearing components whatsoever due to its abysmal heat resistance and tendency to deform under load.

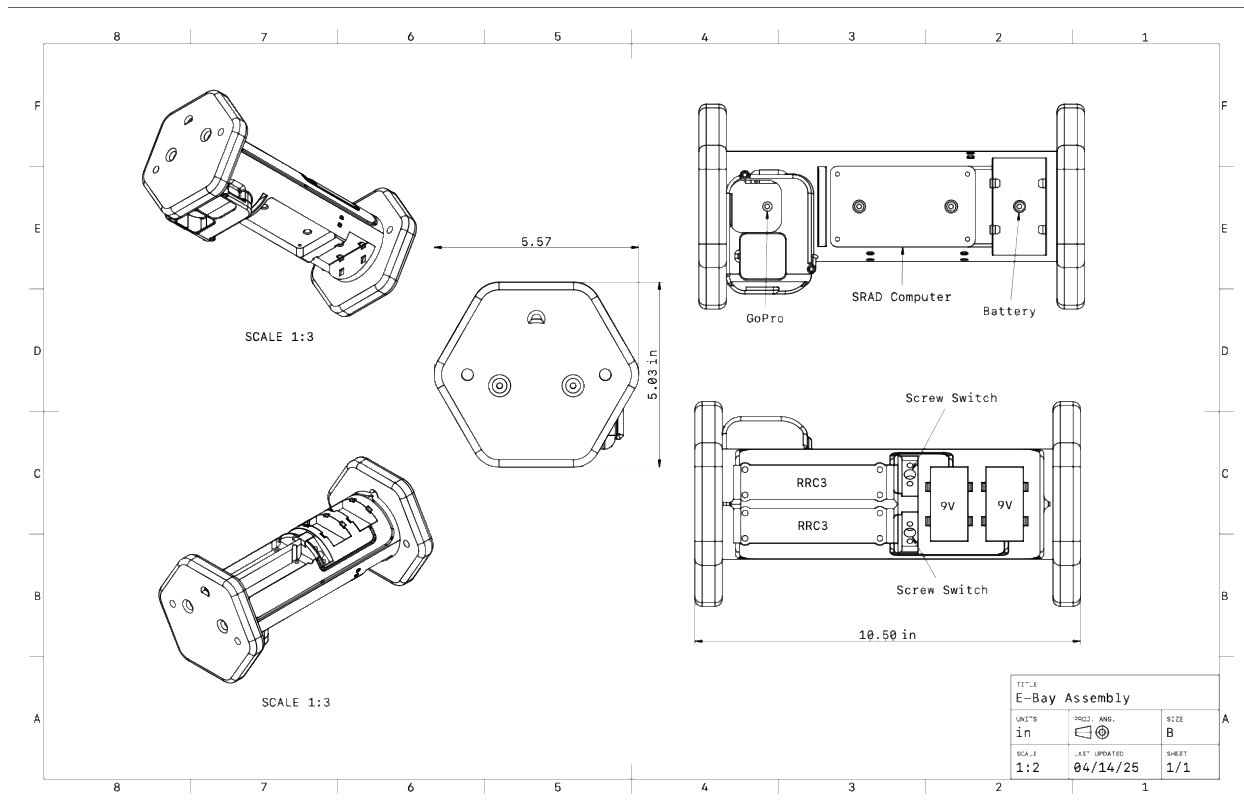


Fig. 32 Primary E-Bay Schematic

II. Mesh Network

The desert proves a challenging environment for sensitive electronics. At Spaceport America Cup 2023, the team's GoPro camera overheated while still on the launch pad. To rectify this, we developed an innovative system for remote camera activation. Since the body of the rocket is RF-blocking carbon fiber, we could not communicate directly with the avionics bay where our GoPro is located. Thus, we developed a 915 MHz mesh network. This network utilizes a ground station node, a relay node in the nosecone (made of RF transparent fiberglass), and an avionics bay node. The avionics bay node activates the GoPro by providing USB power when the command is sent

from the ground station. This system has proven extremely effective for camera activation and has eliminated the overheating issues we faced in 2023.

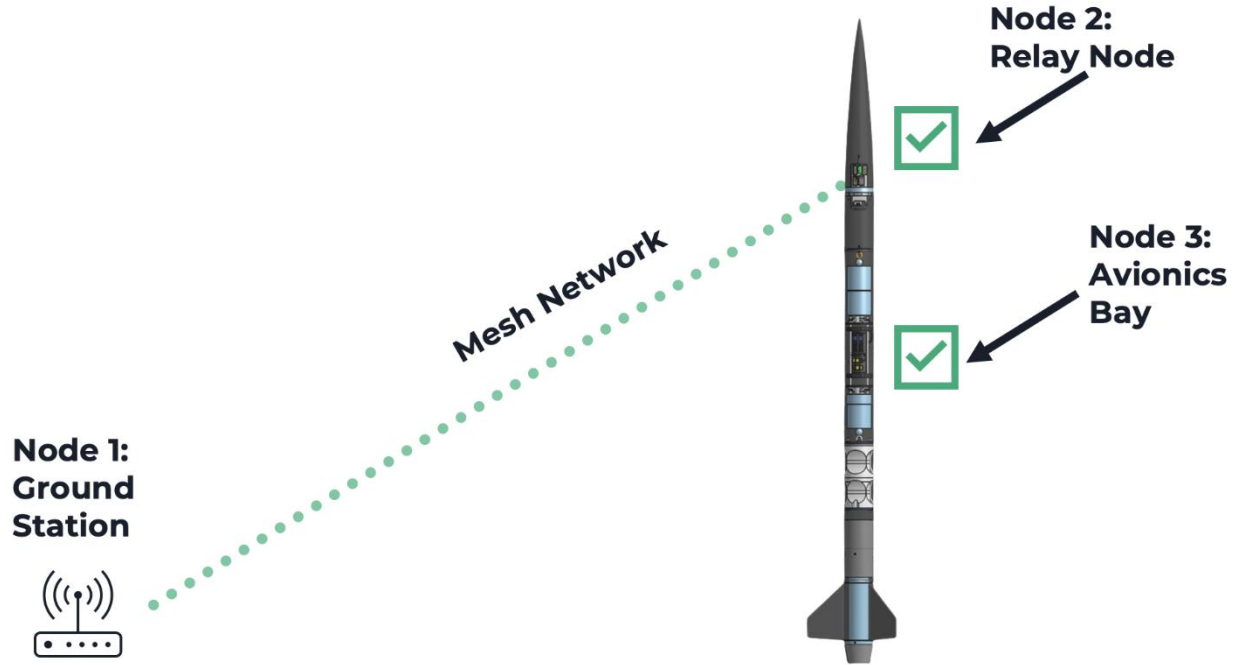


Fig. 33: Network Architecture

Since the system is operational, we have expanded upon it to provide live telemetry back from the sensors in the avionics bay. At the same time, our live video system, if left operational for hours, would likely experience the same overheating concerns our GoPro once did. Thus, we have integrated a MOSFET into the nosecone relay node for remote live video activation. As such, this node is no longer just a relay, as it parses between live video activation packets and packets intended for the avionics bay.

To achieve reliable, low-latency long-distance communication, the team developed a modular software framework using CircuitPython due to its familiar syntax and robust task scheduling, compiling a custom version to support the SRAD flight computer. A simple, expandable packet-based network was created using header bytes to identify sender, receiver, and relay status. Also, instead of using a traditional acknowledgment system, packets are sent cyclically, with the avionics bay responding with a data packet that serves as an acknowledgment. This allows faster command processing, reduced latency, and lower power consumption by enabling nodes to be idle until the ground station is activated just before launch.

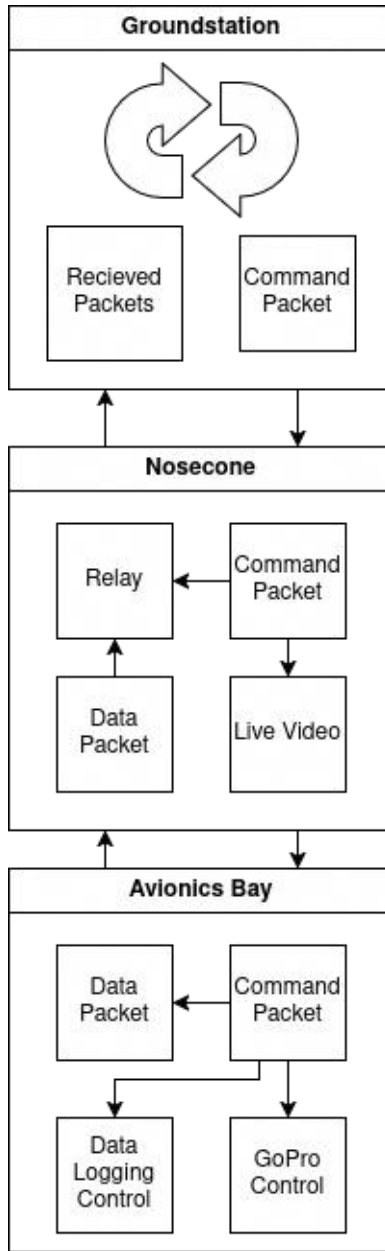


Fig. 34: Network Structure

III.SRAD Flight Computer

Last year we implemented an Adafruit RP2040 RFM915 microcontroller on a custom printed circuit board (PCB) alongside several sensors and power controllers, designated D.A.N. Trinity's flight computer, designated D.A.N. V2, is completely SRAD: instead of attaching different boards onto a larger PCB, it has all components soldered directly to one mainboard in a custom designed system. D.A.N. V2 acts as a transceiver over LoRa communication and collects data on altitude, acceleration, environmental, and gyroscopic. That data is recorded locally on an SD card and transmitted live to the ground station. The board is also capable of boosting battery power to activate the GoPro as well as step-down voltage for system power.

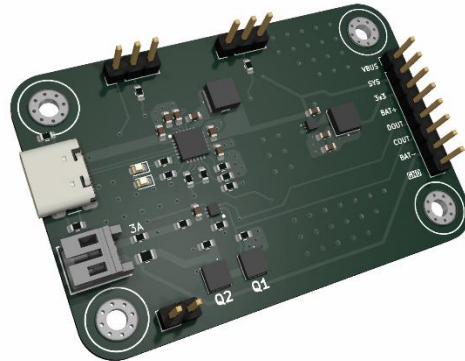


Fig. 35 BMS Board

A significant portion of the custom avionics project involved designing a power supply circuit to handle battery management, charging, and protection. The BMS (battery management system) board above was designed to provide 5V and 3.3V to power circuitry from a single cell Li-Po battery and can charge the battery as well. This system was integrated into the final PCB schematic shown below alongside everything else.

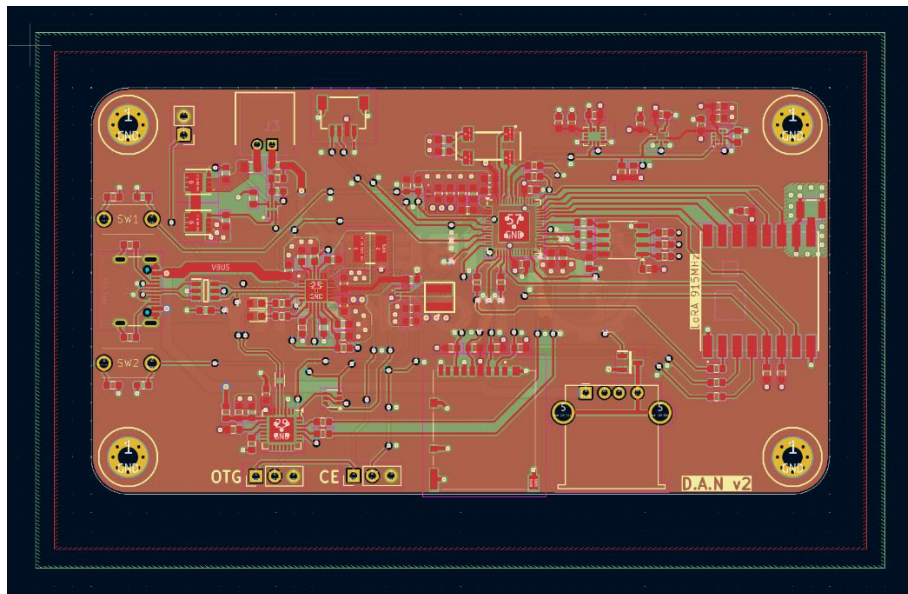


Fig. 36: D.A.N V2 Flight Computer Schematic

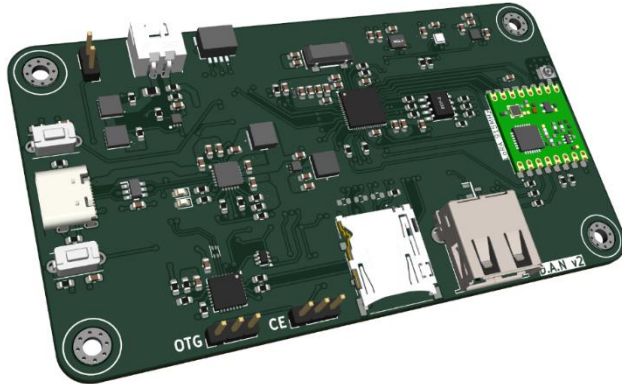


Fig. 37: D.A.N V2 Flight Computer PCB

Trinity's finished SRAD flight computer, D.A.N V2, brings together several sensors, a capable CPU, LoRa networking, and power management onto one board. Building a fully SRAD flight computer allows for functionality that is highly tailored to the team's needs. It includes a 915 MHz LoRa transceiver, a USB-A port for GoPro activation (and the requisite BMS hardware), an accelerometer, gyroscope, barometer, magnetometer, and a SD card for data storage. The 915 MHz transceiver is used to provide live telemetry to the ground station and remotely activate the GoPro. The result of this entire process is a SRAD flight computer that gives the team increased freedom and capability for avionics.

IV. Live Video

Developing a live video system for a high-power rocket is extremely challenging. The live video feed is required to be HD (1080p) at or above 30 fps, with a range of more than 2 miles. Heat generation is also a huge challenge. The SIYI HM30 was chosen as the basis of our live video system. It has great performance at and beyond the required range, its operating temperature is acceptable, and its resolution and framerate are as required. The SIYI HM30 system contains a video transmitter (VTX), camera, several omni-directional antennas, and a receiver. Trinity will utilize the live-video feed output from the receiver. The receiver connects to the ground station computer through a LAN (local area network) wired connection converted to USB. The stream can be viewed on an RTSP stream viewer which connects to our custom GUI (graphical user interface).

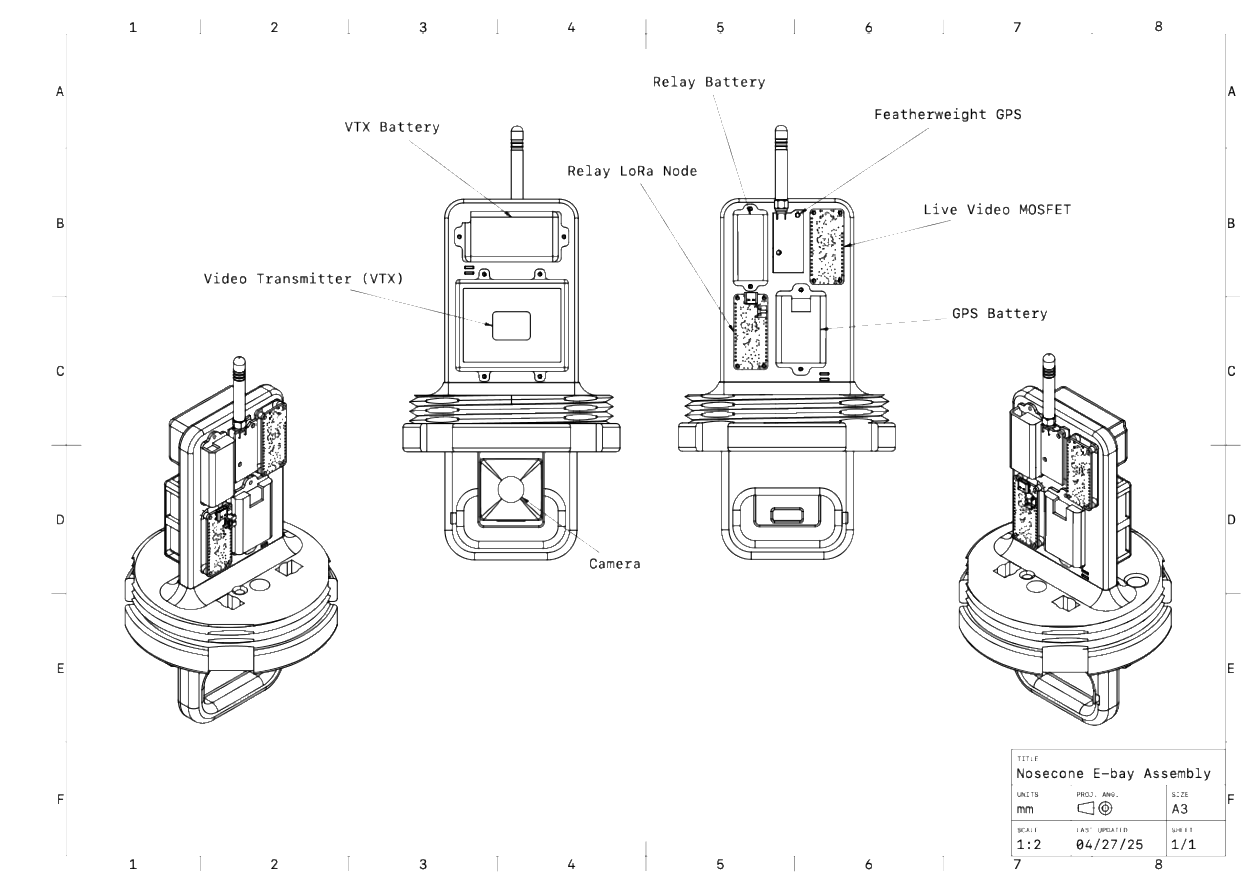


Fig. 38: Nosecone E-bay Schematic

On the rocket, the VTX is mounted in the fiberglass nose cone along with a dedicated LiPo battery and the corresponding 5 dBi omni-directional antennas. The receiver on the ground station side has two 11 dBi directional antennas. Remote activation using a MOSFET wired to the nosecone network microcontroller was implemented to ensure the system would not overheat.



Fig. 39 Live Video Hardware

Extensive testing showed the live video system performed exceptionally, with a tested range of over 3.6 miles, far more than the ~2 miles required at IREC. Crucially, the system reconnected after both units were power cycled. As such, the live video transmitter is only turned on moments before launch. This system resulted in excellent performance at Trinity's first test launch.

V. Ground Station



Fig. 40 Ground Station Computer

For our ground station computer, we require a system that is portable, versatile, and weather and heat resistant. For these reasons the team chose an Apache 3800 case as the foundation. We then implemented a Lenovo ThinkPad X370 laptop and removed the screen. Using a laptop for our ground station is advantageous for a first design, as the built-in battery allows for long runtime when paired with a battery power bank placed underneath the deck. Paired with the laptop is a bright 16-inch 1920 by 1200-pixel monitor. Integrated into the laptop is our Adafruit RP2040 LoRa ground node which is wired to several switches for live video, GoPro, and live telemetry activation. At the same time, the GPS ground station is also wired to the laptop. Finally, the ground station plugs into the live video receiver over a series of ethernet converters. With all systems integrated, the computer has the capability to display live telemetry from the avionics bay, live GPS data, and live video streaming.

To display these components on the screen in a performant and user-friendly way, the team decided to develop the GUI strictly in Python. The team also learned and incorporated proper multithreading into the application to ensure that no process could interfere with another. Live video is simply an RTSP video stream. Smaller tasks like reading data from the featherweight GPS and the custom avionics system are easily handled with basic serial communication libraries. Other tasks, such as connecting and disconnecting from devices, are handled with QT sockets and other routine connection methods. By leveraging these toolkits and methodologies, the team created a UI that met the criteria while remaining easy to develop and maintain.

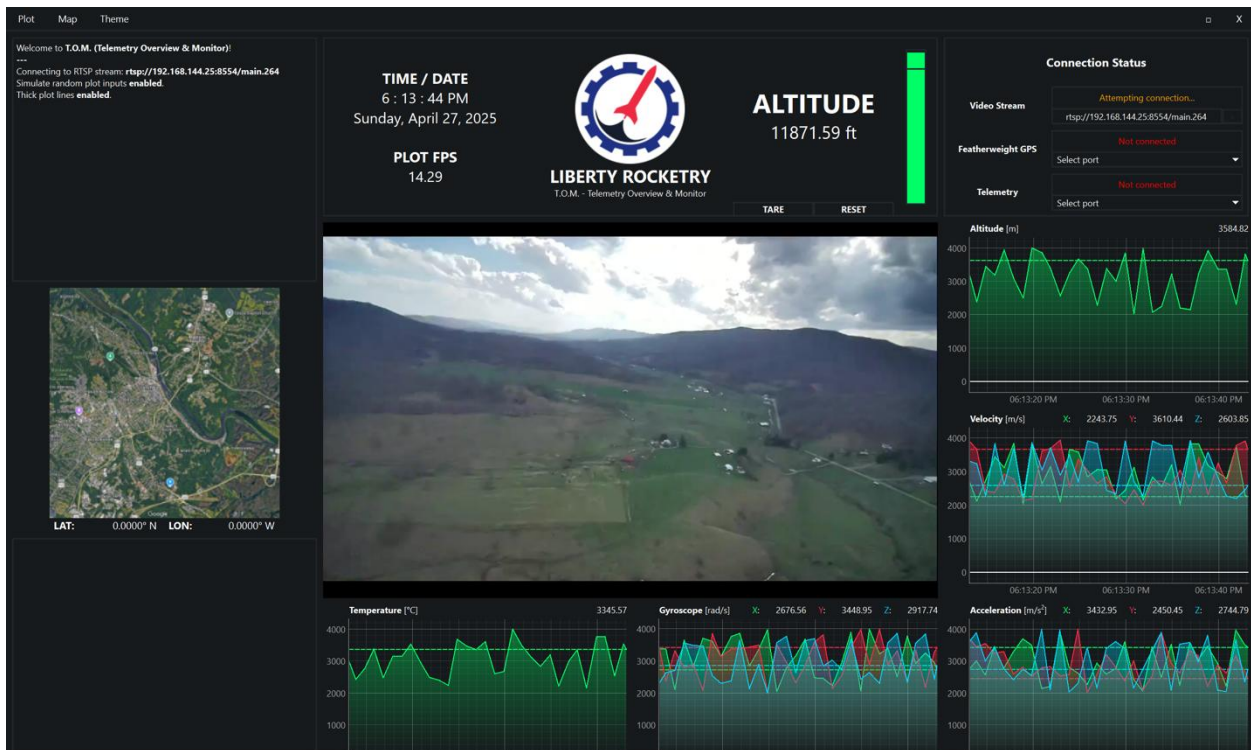


Fig. 41 Ground Station GUI

VI. Experimental Payload

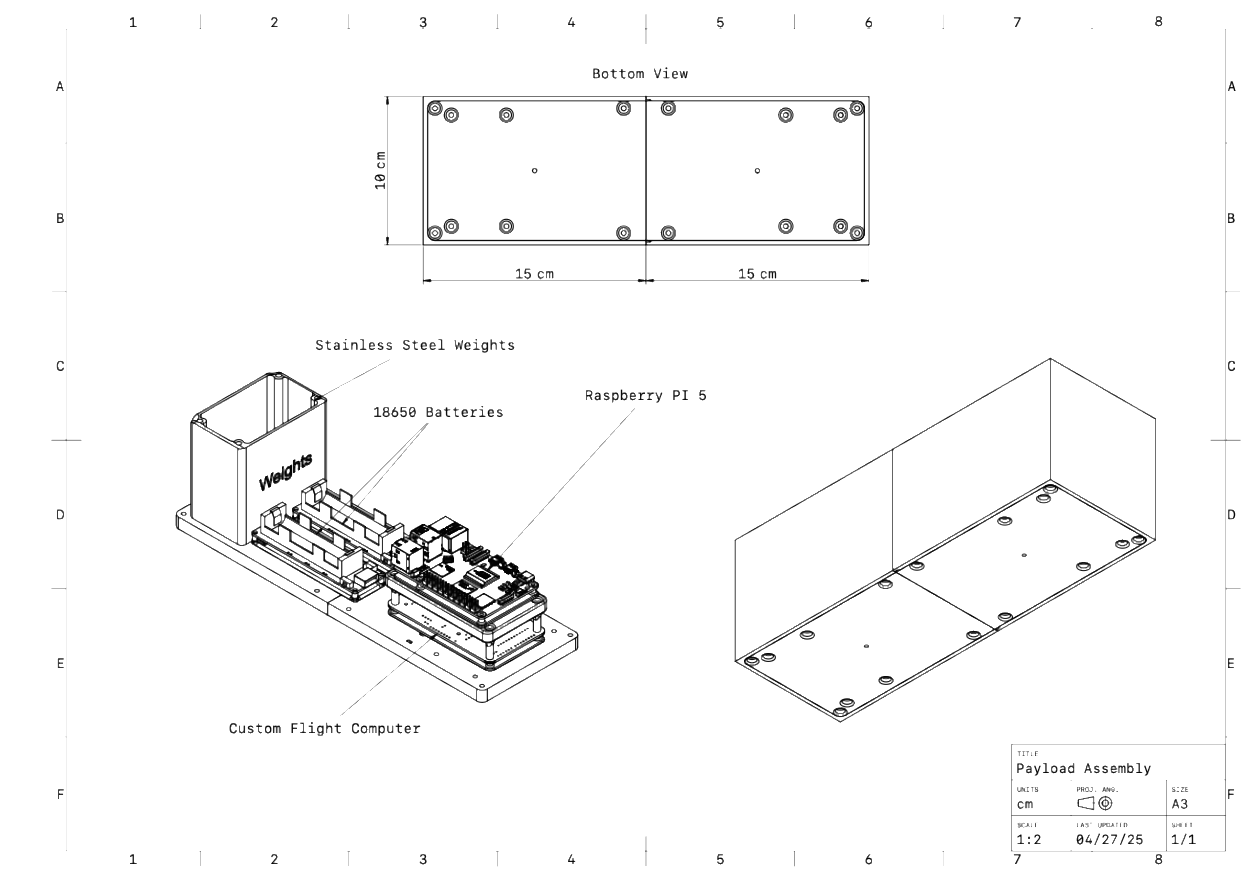


Fig.42 Payload Schematic

6.1 Design Requirements:

A typical projectile flight navigation system will involve both inertial measurement units (IMU's) and global navigation satellite systems (GNSS). Inertial measurement units include accelerometers, barometers, and gyroscopes. GNSS would include GPSs. The problem with GNSS is they may not always be viable due to projectile configuration, signal interference, or cost restrictions, among other reasons. Therefore, a projectile navigation system based solely on IMUs would be advantageous for its reliability and cost-effectiveness. The rise of artificial intelligence (AI) in recent years has allowed projectile navigation via IMUs to be possible. By training an AI model with IMU data as its inputs, it could be able to output reliable and accurate navigation data such as projectile position and velocity. To achieve this, a neural network has been created in Python based on long short-term memory (LSTM) and trained using OpenRocket flight simulation data. The LSTM model will then be implemented on a Raspberry Pi 5 equipped with an AI computing chip and IMU sensors, powered by a single 18650 Li-Ion battery. When the system is loaded on the payload of the rocket, a 30 cm x 10 cm x 10 cm CubeSat, it will record IMU data and attempt to predict the flight path of the rocket in real time.

6.2 Data Formatting and Processing:

To train the LSTM model, input and output variables were selected based on data available in OpenRocket and from the physical IMU sensors. Eight input variables were selected: time, vertical acceleration, lateral acceleration, roll rate, pitch rate, yaw rate, air temperature, and air pressure. Additionally, five output variables were selected: altitude, vertical velocity, lateral distance, lateral direction, and lateral velocity. A simulation time step of 0.01 s was selected in OpenRocket, but the software features a variable time step where the time step is not constant through the duration of the simulation, and there is currently no way to disable this behavior. Eleven simulations were run to generate training data for the LSTM model, and this data was concatenated and then split into training data and labels,

where for each time step the training data is the input variables and the labels are the output variables. These datasets were then normalized and 20% of the dataset was split into a validation set. Next, the data was divided into sequences of length $S_{eq\ len}=20$, and this data was input to PyTorch's Dataset and DataLoader classes with $B_{atch\ size}=10$.

6.3 Model Architecture and Parameters:

To create the LSTM model in Python, PyTorch was utilized. Samples were input to the model as 3-dimensional tensors of size $[B_{atch\ size} \times S_{eq\ len} \times I_{input\ vars}]$, and the architecture was based on a two-layer LSTM with two hidden layer sizes, being $h_1=64$ and $h_2=128$. The architecture can be understood as follows: first, a linear transform was applied to transform the size of the sample's third dimension from size $I_{input\ vars}$ to h_1 . A rectified linear unit (ReLU) was then applied sample-wise as the activation function. Next, the sample was passed to $LSTM_{h1}$, and the outputs of this layer were passed to $LSTM_{h2}$. A dropout function with probability $p=0.2$ was then applied to the sample, which randomly zeroes some of the elements in the sample with probability p to prevent overfitting during training. Finally, a second linear transform was applied to make predictions on the output variables by reducing the number of elements in the sample from size h_2 to $O_{output\ vars}=5$. This framework was then applied on each sample in each sequence and batch size. To update the weights of the network and optimize training, a mean-squared error loss function ($MSELoss$) was used for its suitability for regression problems. The *Adam* optimizer was selected for training optimization with a stepped learning rate that decreases as the number of epochs increases. The learning rate was initialized as $1E-2$ decays by a factor of 0.1 every 20 epochs, resulting in a final learning rate of $1E-7$ for 100 training epochs. This decrease in learning rate is another method used to avoid overfitting the model during training.

6.4 Training Results:

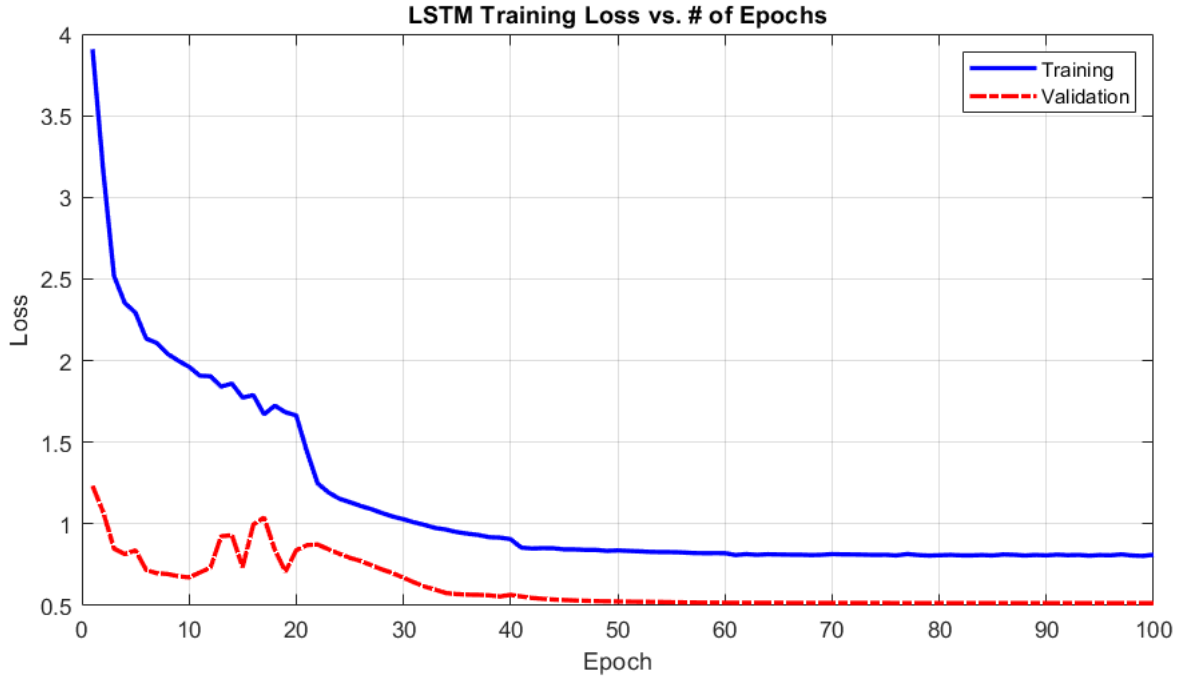


Fig. 43 LSTM Training

The model was trained with 100 epochs run on eleven OpenRocket flight simulations, each with randomized initialization variables within reasonable ranges for the competition launch site. This randomization of initialization variables provides differences in the simulated flight paths, allowing the model to be more robust in its predictions. Batch shuffling was used during training, randomizing the order of the samples in the training dataset for each epoch. When training was complete, the model achieved a minimum training loss of 0.8042 and a minimum validation loss of 0.5151. The decrease in training loss across epochs indicates that the LSTM model successfully learned distinct features and patterns within the data, and the decrease in validation loss indicates that the model became more accurate throughout the duration of the training. Both curves begin to plateau around 50 epochs, indicating that the training may be effective with less epochs, saving time and energy. Due to the stepped decay of the learning rate, the final learning rate was $1E-7$; these steps are also reflected in both loss curves, as the slope of the curve decreases

approximately every 20 epochs. The trained model with its learned parameters can now be exported and imported to the physical hardware inside the rocket payload.

6.5 Conclusion:

An effective IMU-based AI projectile estimation system would allow for key flight variables to be adjusted mid-flight to reach a certain objective, such as applying thrust vectoring or airbrakes to reach a target altitude. This system here is the first step towards these applications. At IREC the model will be inferred in real-time on the flight. For this model, location prediction will be the most interesting result. Without access to a GPS, the model should be able to predict where the rocket is given the launch starting coordinates.

IV. Mission Concept of Operations Overview

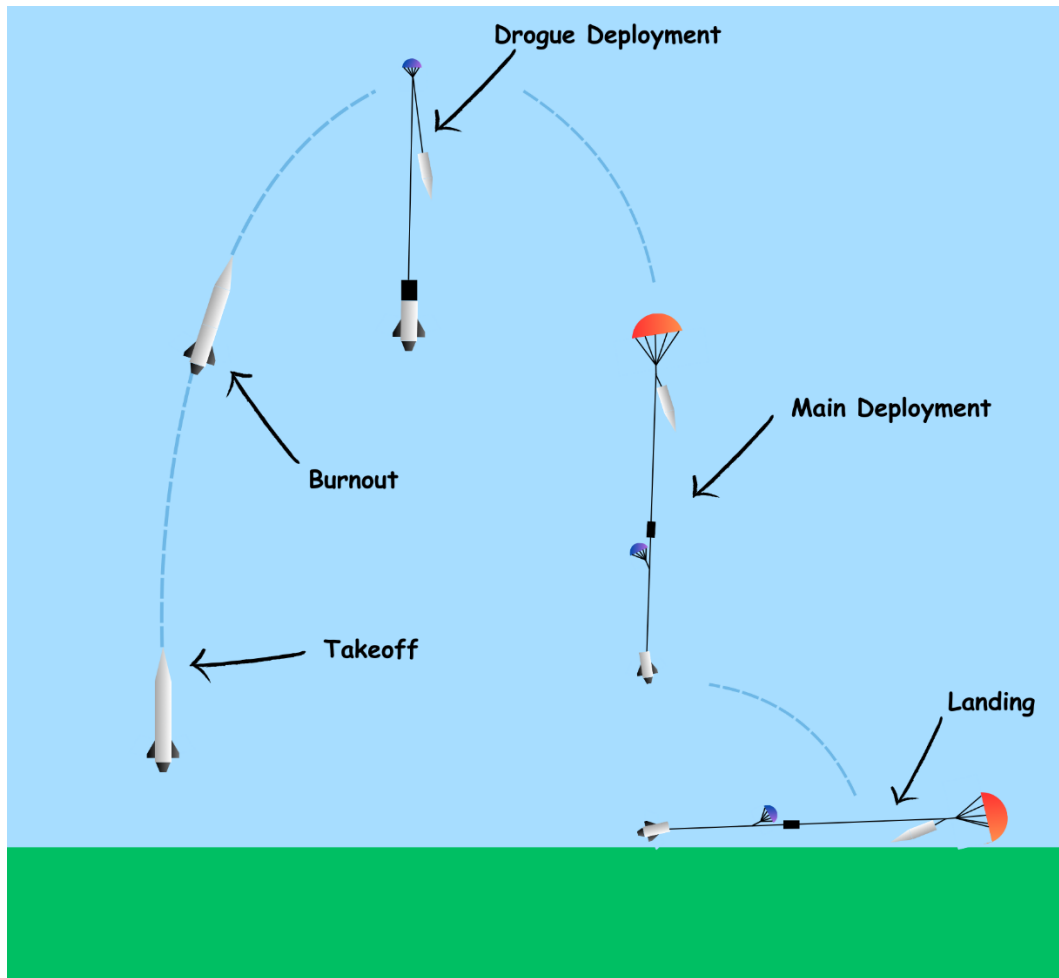


Fig. 44: Trinity Mission Overview

4.1 Definitions

There are seven major events, or mission phases, in Trinity's solid rocket launch. To successfully execute these events, there are four control subsystems, defined in Table 5. The mission phases are as follows: System Arming, Ignition, Takeoff, Engine Burnout, Apogee, Main, and Landing. These phases are outlined and defined in 4.2 – Mission Phase Descriptions.

Definitions		
<u>System</u>	<u>Designation</u>	<u>Description</u>
Propulsion	SF	APCP Solid Fuel
Ignition	EM	Ematch Ignitors
Recovery	RD	Parachutes, Charges
Avionics	AS	Altimeters, Switches

Table 5: Control Subsystem Definitions

4.2 Mission Phase Descriptions

System Arming			
<u>SYSTEM</u>	<u>STATUS</u>	<u>STATE</u>	<u>Description</u>
SF	Safe	Unused	Solid Fuel - Unignited
EM	SAFE	Unused	Connected to starter
AS	ARMED	Powered	System Armed, Switch On, Altimeter in Standby

Ignition			
<u>SYSTEM</u>	<u>STATUS</u>	<u>STATE</u>	<u>Description</u>
SF	ARMED	POWERED	Solid Fuel - Burning
EM	ARMED	POWERED	Ignited
AS	ARMED	Powered	Standby

Takeoff			
<u>SYSTEM</u>	<u>STATUS</u>	<u>STATE</u>	<u>Description</u>
SF	ARMED	POWERED	Solid Fuel - Burning
EM	Safe	Used	Ignitor burned up
AS	ARMED	Powered	Standby

Engine Burnout			
<u>SYSTEM</u>	<u>STATUS</u>	<u>STATE</u>	<u>Description</u>
SF	Safe	Used	Solid Fuel - burned up
EM	Safe	Used	Ignitor burned up
AS	ARMED	Powered	Standby

Apogee			
<u>SYSTEM</u>	<u>STATUS</u>	<u>STATE</u>	<u>Description</u>
SF	Safe	Used	Solid Fuel - burned up
EM	Safe	Used	Ignitor burned up

AS	ARMED	Powered	Eject Drogue Parachutes, (2/4 charges now used)
----	-------	---------	---

Main			
<u>SYSTEM</u>	<u>STATUS</u>	<u>STATE</u>	<u>Description</u>
SF	Safe	Used	Solid Fuel - burned up
EM	Safe	Used	Ignitor burned up
AS	ARMED	Powered	Eject Main Parachutes, (4/4 charges now used)

Landing			
<u>SYSTEM</u>	<u>STATUS</u>	<u>STATE</u>	<u>Description</u>
SF	Safe	Used	Solid Fuel - burned up
EM	Safe	Used	Ignitor burned up
AS	Safe	Powered	Eject Main Parachutes, (4/4 charges now used)

Table 6: Mission Phases

V. Conclusion

Trinity was the third rocket designed and manufactured by Liberty Rocketry since the teams founding four years ago. The team has been able to do a lot in those four years from building its first rocket, earning a spot in the top ten, designing unique avionics hardware, and manufacturing a custom boat tail. This year has been another successful year and we are excited for the future of the team. With that said, here are some of the ways Liberty Rocketry is looking to grow.

Designing a rocket can have varying degrees of difficulty, in the end, how difficult the design phase of the rocket is can be dependent on how ambitious the team wants to get. In our first two years of competition, the team was able to learn a lot about high-power rocketry without a lot of failures thanks to incredible Tripoli advisors. This did two things for the team: allowed us to build high quality rockets that performed well and build a large team. While both of these achievements are desirable, they do have some negative side effects. Failure drives development, it pushes the team to either get better or quit. For our team, we have been able to avoid the more catastrophic failures. Out of 6 launches, only one has had a main deployment failure. We have never broken a fin, cracked a fillet, or ripped a parachute. As we start designing our fourth rocket, it is important for the team to acknowledge the small failures in hopes of avoiding the large ones. One of the more subtle challenges that the team will face in the future is a tendency by teams to plateau. The team can naturally start to repeat what has already been done and to not pursue further development. One of our lessons that we have learned this year is to make goals that are reasonable and following through with them. Presenting to the team solid goals every year will encourage members to keep striving with a good task ahead of them. This causes an increase in development without burning out the team or plateauing.

Knowledge transfer is highly important to a team's growth and development. Without good knowledge transfer, a team can risk stagnating as mistakes get repeated and failures stack up. This is even more common in competition teams than in the business world because of students graduating and moving on. On average, a member may only be a part of the team for three or four years. If one or two of those years are spent relearning knowledge the team already possessed, it can be wasted potential. Our leadership structure is done so in a way to fix this by having third year students lead the team. This way, once they are done, they still have a year at school to advise the next generation of leaders before they graduate. One of the lessons our team is learning is what is the best way to pass down knowledge. To help pass down knowledge, each section of our team has a knowledge bank that freshman

learn each year. On top of that, we built a wiki this year to house the increasing database of what the team has learned over the years. For manufacturing, the team created a manual that details the main manufacturing of the rocket. Next year, the team hopes to continue working on knowledge transfer in an effort to continue to grow the team.

APPENDIX

a) Recovery System Testing

1.1 Black Powder Testing

It is of upmost importance that the rocket separates when triggered or else the recovery system will not be released, and the rocket will plummet to the surface of the earth. To ensure that this does not occur, ground tests were conducted. Black powder is used to separate the rocket airframe by igniting with an e-match and building pressure in the parachute bay from the reaction. This pressure forces push the airframe apart while shearing the nylon screws that temporarily keep the airframe in one piece. The result is just enough black powder so that the separation isn't too violent but not lacking in force to ensure full separation. For the drogue chute it was decided that the primary charge will be 2 g and a secondary of 2.5 g. For the main chute the primary charge is 3 g with a secondary of 3.5 g.

With these numbers, ground ejection tests can be conducted to ensure proper separation during competition. Charges were prepared by taking the pre-determined amount of black powder and an e-match and stuffing them into a latex finger cot. The neck of the finger cot is then zip tied closed to prevent spilling the black powder and to allow for the gasses to initially build for a more complete burn when triggered. The parachutes and tethers are then loaded into their designated compartments. Next, the charges are loaded into the charge wells and taped over to hold them in place during the test. The wires of the e-matches are guided through the rocket and led out through the opening for the GoPro (Keep in mind that the avionics bay is empty of electronics and only holds a dummy weight in its place). The airframe sections are then put together and secured with shear pins. The fully assembled rocket for ground ejection test is then leaned again a wooded support to keep it in position during the test. A backstop is placed at the tail of the rocket to prevent it from moving backward when the black powder is ignited.



Figure 45: Main Parachute Black Powder Separation Test

Without a battery connected, the wires of one of the charge wells are connected to the detonator. Finally, with everyone at a safe distance and angle relative to the rocket. A battery is then connected to the detonator for ignition. Finally, the detonator switch is flipped, and the black powder charge is ignited. The pressure builds and forces the airframe sections apart while shearing the nylon shear pins. As the airframe sections are moving away from each other, they also aid the release of the parachutes and tethers allowing proper deployment in a real flight. A total of six tests were conducted, and both the main and redundant charge sizes were tested to ensure every size was adequate. Each test resulted in successful deployment of the system including the release of the drogue and main parachutes. Also, there was no major tangling among the systems components.

1.2 Recovery Drop Testing

One major concern our team had was with our shear pins and the possibility of a premature main deployment. When the drogue deploys at apogee, the calculated snatch forces the parachute puts on the rocket could break our main parachute shear pins and result in a premature main deployment. To test the impulse our shear pins could withstand before breaking, we prepared a specialized drop test and a MATLAB file to calculate the impulse. This testing allowed our team to determine if there would be premature separation and if more shear pins were needed.



Figure 45: Image of Drop Test

Using the nosecone section and the avionics bay (filled with dummy weight), the impulse our system experiences at apogee could be replicated. The avionics bay was connected to the nosecone by a shorter tether as a failsafe in case the shear pins broke, and the other end was connected to the bridge. The system was tested by dropping the front section off the bridge at an off campus engineering lab and calculating the snatch from the tether. The tether was attached via the custom recovery yoke and the length it was dropped was measured out before the test was conducted.

Following this set of tests, calculations were made and analyzed after conducting the drop tests where the average force on the main bay shear pins was determined. To accomplish this, the velocity of the drop was found by calculating change in distance over change in time. This was then used to find the impulse. The time of impact was used along with the velocity to find the average force on the shear pins. With six 4-40 shear pins, we were able to successfully perform a drop test. The shear pins successfully held the rocket together at the required impulse with a high factor of safety. The calculations made to determine the velocity, impulse, and average force experienced is shown below in Figure 46.

Mass		7.849 kg	Force Using SI Calculations			
Change in Position (m)	Velocity (m/s)	Impulse (kg-m/s)	Time Force is Acting Over (s)	Force (N)	Force (lbf)	Broke?
0.9144	4.235626046	37.28903747	0.03	2442.968	549.201	Y
0.61	3.459508636	59.85987792	0.03	1995.329	448.568	N
0.762	3.866579884	66.90343173	0.03	2230.114	501.350	N (only one)
1.524	5.468169712	94.61574053	0.04	2365.394	531.762	Y

Fig. 46: Drop Test Calculations

Custom Recovery Yoke Analysis and Simulations

Purpose of the Yoke

The avionics bay is the central section of the rocket that connects both the front and rear sections of the rocket. It is sandwiched between two G-10 fiberglass bulk heads and secured together with two 5/16 inch aluminum rods. When the rocket reaches the target altitude for drogue deployment, the rocket then separates, releasing the drogue chute. The initial snatch force and following drag forces are directly applied to the threaded rods connecting the avionics bay. In previous years the avionics bay was fastened via I-bolts that were threaded on the ends of the rods and a tether looped between them. The problem with this design is that when a tensile force is exerted on the tether,

which is looped through both of the I-bolts, the tether creates a triangle between the two. That means a component of the vertical tensile force is translated as a horizontal force pulling the I-bolts together, towards the center of the bulkhead. When a great enough force is exerted through the tether, the screws became slightly bent and deformed. This is more concerning when considering the possibility of the main chute prematurely deploying at the wrong altitude or with too much speed. Since the main chute is much larger than the drogue chute it will exert a higher shock and drag force on the I-bolts and subsequent threaded rods. If the force was applied equally to the screws axially, then there would be no concern for bending. However, because the I-bolts are pulled horizontally together in a bending/shear fashion, the threaded rods cannot withstand such forces and are permanently deformed. This problem was discovered through drop testing of the rocket, with original intent to ensure that premature shearing and chute deployment wouldn't occur before required.

Design Process

To combat the issue of the threaded rods bending, a solution to evenly distribute the load on both screws in an axial manner was devised. The solution to this was to design a load distributing tether attachment bar, which we call the yoke. The yoke would connect the two threaded rods together with a central attachment point at the center for the tether. This way the bar takes the tensile load, and without excessive bending or flexing, it axially applies it to both screws avoiding excessive bending or shear forces exerted on the threaded rods.

The yoke wasn't designed with specific metrics in mind. The only parameters were that it needed to fit within the bulkhead and be able to withstand the maximum theoretical loads that would be applied without excessive bending or flexing. It is designed for the threaded rods to feed through holes in ends of the yoke and tightened down with nuts. An arbitrary thickness of 0.5 inches was set for the regions of the threaded rod fasten points. The overall length of the bar needed to fit within the diameter of the bulkhead while reaching each threaded rod came to a length of 4.6 inches, refer to figure 1 and 2. To keep things proportional an extruded thickness of 0.5 inches was applied. To securely hold a tether, a gap with rounded edges was modeled for ease of assembly and to reduce the risk of friction and tearing. All other values used to in the design were chosen because they were relatively even numbers that could easily be machined.

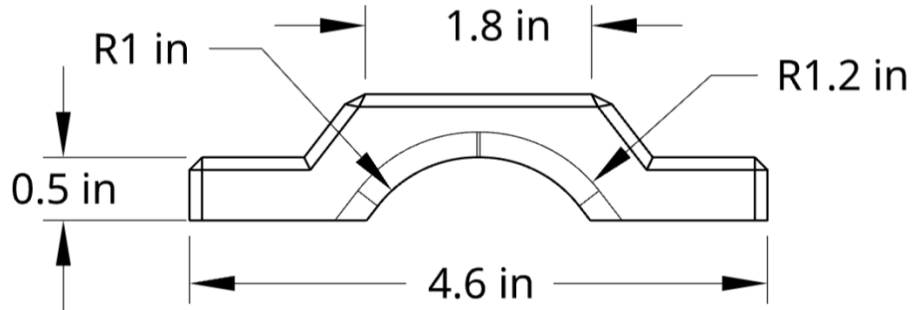


Fig. 47: Side Profile Engineering Drawing of the Yoke

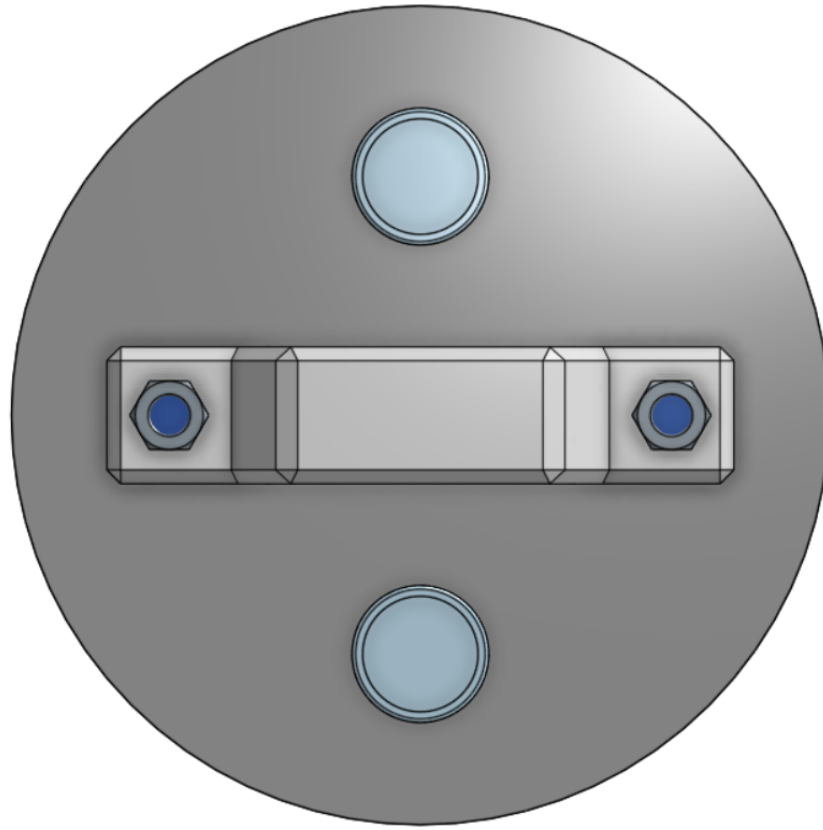


Fig. 48: Top-Down View of Bulkhead with the Yoke Attached

When choosing the material, the yoke was going to be manufactured from, there were parameters to consider. Firstly, it needed to be made of material that was inexpensive and easily manufacturable. The material needed to be relatively lightweight and heat resistant. It also needed a decent strength to weight ratio, especially one on the more ductile side. The material chose for the yoke was 6061 Aluminum. This was primarily chosen because it fit all of the parameters previously outlined, but mostly because it was one a few available through the chosen manufacturer.

Before finalizing the design and sending for it to be manufactured, simulations were conducted to ensure it met each requirement. Using Onshape's built-in simulation and ANSYS, it was concluded that the design outperformed each requirement by a large margin. The total displacement expected under 4,000 lbf of load was only 0.267 mm or 1.028e-2 inches.

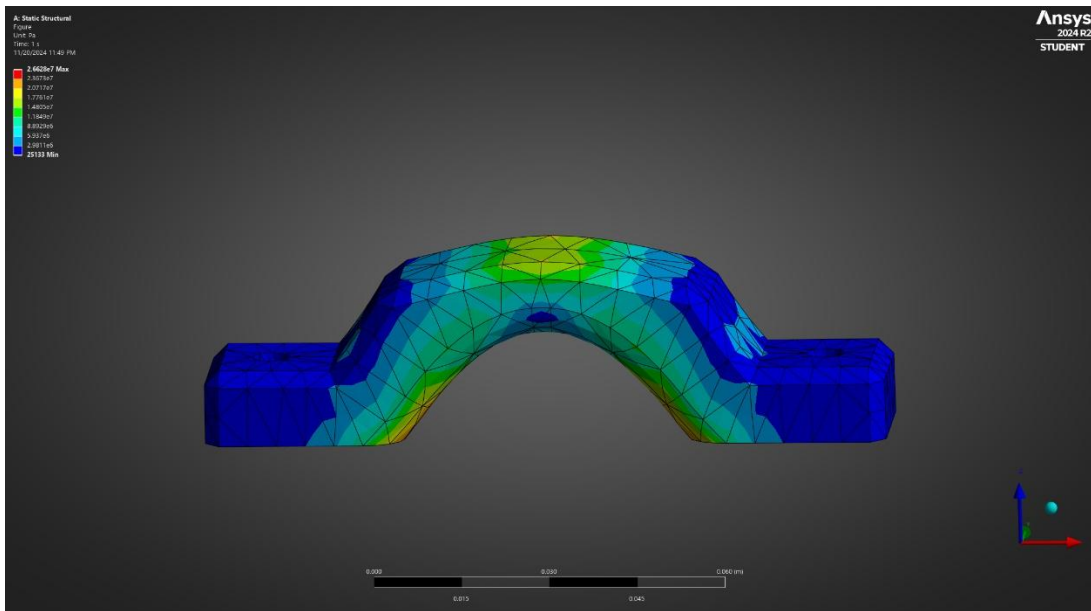


Fig. 49: Ansys Static Stress Simulation of the Yoke

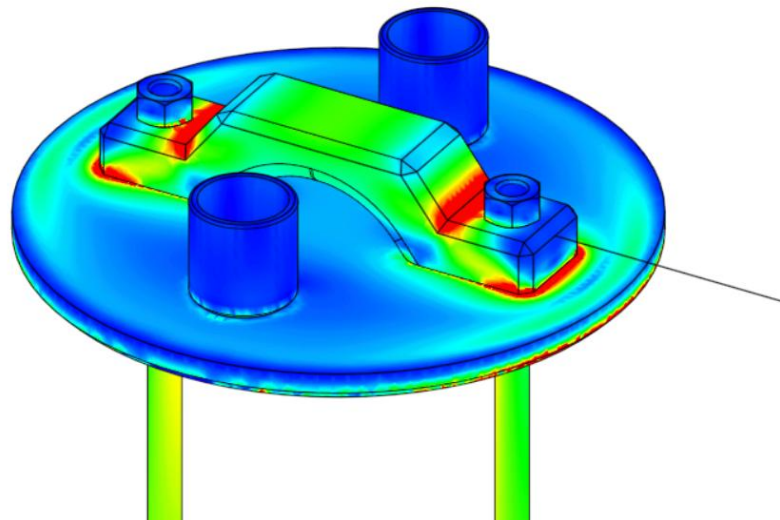
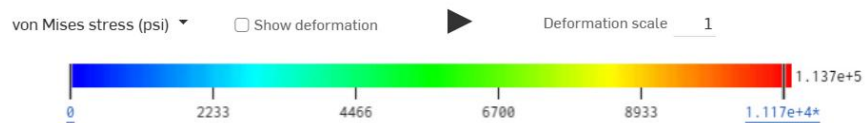


Fig. 50: Onshape Static Stress Simulation of the Yoke

G10 Fiberglass Bulkhead Analysis

1. Introduction

G10 Fiberglass is a composite material, which is a material produced from two or more constituent materials. These constituents have notably dissimilar chemical/physical properties and are merged to create a material with properties unlike the individual elements. Within the finished structure, the individual elements remain separate and distinct, unlike mixtures. This material serves as our bulkheads in the rocket, which are crucial structural points for our recovery system. The purpose of this report is to analyze the material properties of COTS G10 Fiberglass to perform better and more accurate simulations for future recovery designs.

2. Materials and Methods

2.1 Sample Sizing and Cutting

A 12" x 24", 1/4" Thick, Blue Flame-Retardant Garolite G-10/FR4 Sheet was bought from McMaster-Carr (85345K424). This is a slight decrease in thickness compared to past rocket sizes which used 3/8" thick bulkheads. To gain the most accurate data possible our team utilized two ASTM standards, D3039/D3039M – 17 standards for tensile testing and ASTM D790-17 for three-point bend testing. Due to the high risk of delamination that can come with manually cutting samples, our team utilized a OMAX waterjet to cut out 4" x 1/2" x 1/4" samples. Initially, the wrong thickness was inputted into the machine, resulting in three poor samples. These samples had extremely rough edges, however we utilized these samples in initial testing to ensure the correct setup was used, before we started to record data. There were three orientations of samples we had cut out of the G-10 fiberglass, 0°, 45°, and 90°. A visual of these orientations can be shown below.

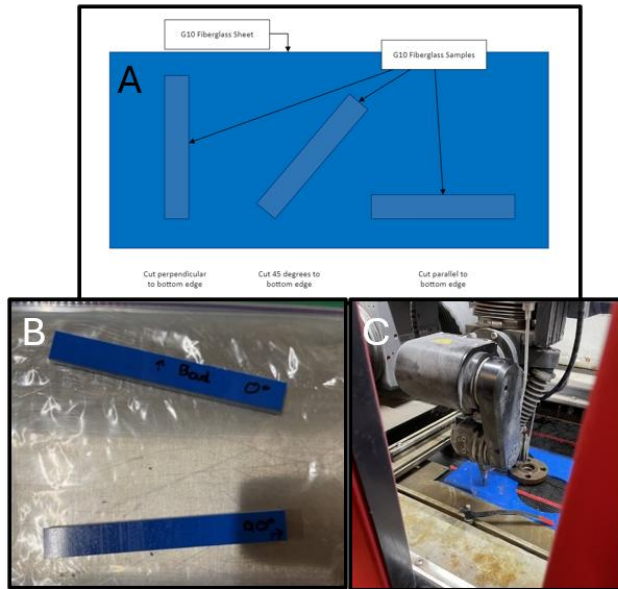


Fig. 51: A) Orientation of Fiberglass samples. B) A bad sample (top) and a good sample (bottom). C) Samples being cut out with the waterjet

2.2 Tensile Testing

All tensile testing was done with an Instron 5982 load frame using two 2716-003 Manual Wedge Action grips for tensile testing, alongside ASTM D3039/D3039M – 17 standards. A crosshead rate of 2 mm/min was used for all tensile tests. Initially, a preliminary test was performed on a sacrificial sample to ensure optimal grip tension on the fiberglass surface. Despite our efforts, the sample fractured approximately 2mm below the top grip. Subsequent tests were conducted with varying grip strengths and alignment adjustments yet yielded consistent outcomes. Due to concerns regarding potential stress concentration at the grips and its impact on data integrity, the results from these trials were excluded from all future analysis. Upon careful reflection on the overlooked issues, detailed in the results section, our team decided to transition to a three-point bend test methodology. This approach was deemed more reflective of the real-world stresses our bulkheads would endure within our recovery system. Moreover, it offers a more accurate simulation of the forces acting upon our bulkheads.

2.3 Three Point Bend Testing

The same Instron 5982 load frame was utilized alongside a 100 kN flexure fixture. In addition, the same sample sizing was utilized for simplicity and consistency for future testing. The flexure fixture had a separation distance of 100 mm, and the samples were placed centered to the center of the fixture. A max condition of 100 kN was applied, however the samples tested never exceeded that value. Then by using the control panel the machine has was moved until the top metal cylinder rested very lightly on the specimen. Subsequently the machine's displacement was set to zero. After that the test was started and the machine measured variables such as flexural stress, strain, force, and displacement.

2.4 Characterization

A few selected samples, following the compression tests, were wet ground by hand using progressively finer SiC abrasive papers culminating with 1200 grit. A Keyence VK-X1000 optical microscope was used to image the sample surface and assess fiber structure and orientation post bending test.

3. Results

3.1 Mechanical Property Comparison of the Fiber Orientations

The following data was graphed to show the comparison of the sets of samples. Due to little variation in each test conducted, as shown in the Figure below, comparison between fiber orientations will be simplified to one sample in each orientation.

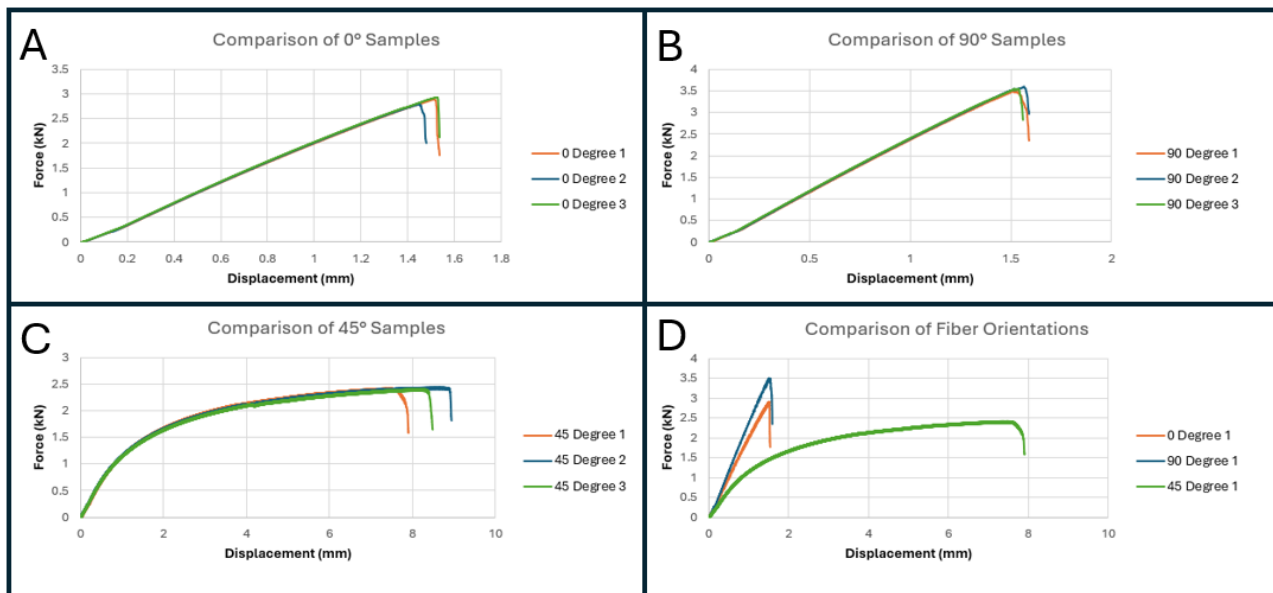


Fig. 52: A) Comparison of 0 degree orientation; B) Comparison of 90 degree orientation; C) Comparison of 45 degree orientation; D) Comparison of all orientations

The specimens oriented at 0° exhibited an average displacement of approximately 1.4933 \pm 0.00 mm. Similarly, samples oriented at 90° displayed a comparable pattern, with an average displacement of 1.5385 \pm 0.026 mm. Notably, the 90° orientation demonstrated a significant increase in maximum force, measuring around 3.5307 \pm 0.028 mm. This represents a 23.36% rise from the maximum force recorded for the 0° orientation, which stood at 2.8622 kN. Conversely, specimens oriented at 45° showcased a substantial deviation from both the 0° and 90° samples. These exhibited a maximum force of only 2.4019 kN and a corresponding displacement of 8.0135 mm, representing a 16.0% decrease in maximum force and a 55.94% increase in displacement compared to the 0° orientation.

Table 7: Comparison of Maximum forces and corresponding displacement for each tested sample.

Orientation	Maximum Force (kN)	Corresponding Displacement (mm)
0° Sample 1	2.8921	1.5116
0° Sample 2	2.7752	1.4443
0° Sample 3	2.9194	1.5254
90° Sample 1	3.4882	1.5229
90° Sample 2	3.5791	1.5672
90° Sample 3	3.5248	1.534
45° Sample 1	2.4001	7.3579
45° Sample 1	2.4191	8.5577
45° Sample 1	2.3866	8.1249

The high variation between 0° and 90°, and 45° samples can be attributed to both the fiber structure and orientation of the fibers. As we can see below, the orientation of the fibers follows a 0° and 90° pattern, or a bidirectional pattern. Therefore, when the force was applied on the 0° and 90° orientations, the force was placed directly on the fibers, which caused a sudden break. On the other hand, the force applied to the 45° orientation did not exert direct pressure on the fibers, affording greater flexibility and leading to a significantly higher displacement, albeit with a lower overall maximum force.

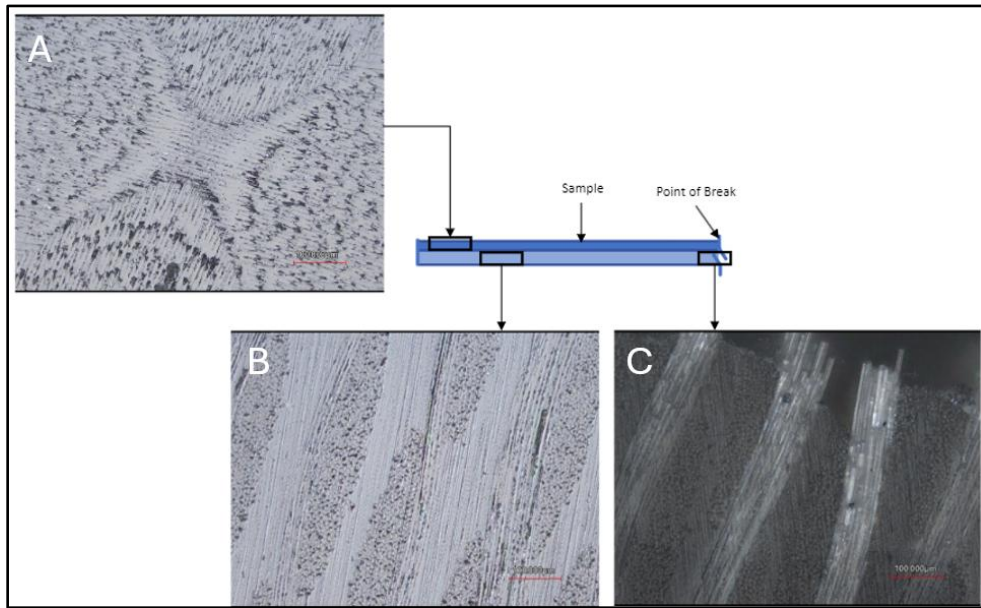


Fig. 53: A) Polished Top View of sample; B) Cross Section view of 0° sample; C) Cross-sectional view of 0° sample break point

Our group also plotted our stress-strain curves for each sample. First, we calculated a theoretical stress and strain value for our samples. Assuming we have a cross-sectional area of $A_o = 0.000080645m^2$ and an applied force of $F = 2862.233N$. We utilized the following equations to find a flexural stress of $\sigma_f = 396.39MPa$ and a flexural strain of $\epsilon_f = 0.025$.

$$\sigma_f = \frac{3FL}{2bd^2} \quad \epsilon_f = \frac{6Dd}{L^2}$$

The stress for all three orientations had a percent difference of ~1.35% and the strain had a percent difference of only 0.695%.

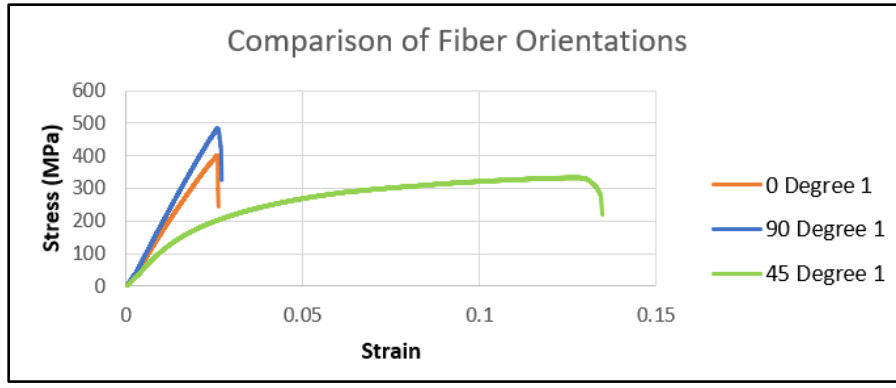


Fig. 54: Comparison of all Fiber Orientations

3.2 Finding SolidWorks Data

With this information in mind, the data was analyzed using SolidWorks. SolidWorks Finite Element Analysis (FEA) Simulations on average need three parameters for the simulation to function properly, Young's Modulus, Poisson's Ratio, and Yield strength [5]. Young's Modulus is the tensile or compressive stiffness when a force is applied lengthwise on a material. Poisson's ratio is the negative of the ratio of transverse strain to lateral or axial strain. And the yield strength represents the upper limit to forces that can be applied without producing permanent deformation in a material. For brittle materials, the yield strength is also defined to be where the sample breaks, since most brittle materials exhibit little to no deformation before failure. First, the raw data from the Instron was exported to Excel, so that it may be utilized for these calculations.

3.2.1 Young's Modulus

Due to our testing being accomplished via three-point bend tests, Young's Modulus has several equations associated with this test to account for the central deflection created. Young's Modulus can be calculated via the following equations, obtained from [6].

$$W_0 = \frac{PL^3}{48EI} \quad I = \frac{a^3b}{12}$$

Where E is Young's Modulus, I is the second moment, P is the applied force, and L is the separation distance between the fixture points. By plugging in our values from our tests, Young's Modulus was found to be $E_0 = 15.32 \text{ GPa}$, $E_{90} = 17.55 \text{ GPa}$, and $E_{45} = 2.30 \text{ GPa}$.

3.2.2 Poisson's Ratio

Poisson's Ratio is calculated from tensile tests, using extensometers. Since the samples failed during tensile testing, Poisson's Ratio will be obtained from other research data. There were three main articles viewed to determine the best Poisson's ratio to use. Kasen et. Al. [7], Vogel et. Al. [8], and Steinburg's novel [9], all tested mechanical properties of woven G10 fiberglass, or fiberglass composites. [7] found a range of values, from 0.144 to 0.215. These values were taken as a comparison of temperatures, so it is best to choose the ratio found at room temperature, or 0.144. Values from [8] ranged from around 0.1 to a little under 0.5. Finally, Steinburg's novel [9] found Poisson's ratio to be 0.12. Because of the similarity found between the tested data in [7] and our data, .144 was chosen to be Poisson's ratio the simulations. The minimum value was chosen as well, because if the simulations showed the bulkheads withstanding the forces at a lower Poisson's ratio, then it can be guaranteed they will withstand at higher rates.

3.2.3 Yield Strength

Yield strength occurred at the maximum stress in each sample, $\sigma_0 = 392.32 \text{ MPa}$, $\sigma_{90} = 470.30 \text{ MPa}$, and $\sigma_{45} = 320.02 \text{ MPa}$.

3.3 SolidWorks Modeling

The SolidWorks model included a very basic design and setup to prevent any major complications. There were several iterations that we went through to compare and provide the most accurate model. To start, a simple eyebolt in a bulkhead was utilized, and the system was slowly built into a full, accurate model. Throughout this iterative process, simulations were conducted with certain assumptions to streamline the model, deliberately omitting various factors. These assumptions will be rationalized as necessary. All bulkheads had a fixture on the outer diameter of the bulkhead, reflecting how our bulkhead is secured with epoxy inside the rocket. And all simulations were accomplished with SolidWorks Static simulations.

3.3.1 Shock Force

The force utilized in our simulations is also known as shock force in rocketry. All simulations utilized a force of 2200N (or 500lbf). This shock force chosen was the average force across different parachute designs that was experienced over the years. Which is what we had initially calculated from our shock force calculations for our main parachute. It was determined later that the actual force was lower than the initial calculation, meaning the bulkheads chosen are well within standards. The shock force can be calculated using the following equations:

$$F = \frac{1}{2} C_k (C_D S)_0 \rho v^2$$

3.3.2 Meshing

Initially, the eyebolt had threaded built into the model. However, this model had several elements with high aspect ratios. According to the SolidWorks website, it is advised for complex models to have a low maximum aspect ratio, alongside a percentage of at least 90% for percentage of elements with Aspect ratio $< 3'$. As seen in the image below, while there is a high percentage of elements with a low aspect ratio, the maximum aspect ratio was extremely high. This high ratio can affect the accuracy of the simulations to follow.

Mesh Details	
Study name	Iteration 3 (-Defa
Total nodes	96829
Total elements	57869
Maximum Aspect Ratio	65.552
Percentage of elements with Aspect Ratio $< 3'$	96.4
Percentage of elements with Aspect Ratio > 10	1.87
Percentage of distorted elements	0
Number of distorted elements	0
Remesh failed parts independently	Off
Time to complete mesh(hh:mm:ss)	00:00:34
Computer name	

Fig. 55: Meshing Details

To lower the maximum aspect ratio, it is often advised that certain structures of the model should be reduced or simplified. Structures such as fillets, chamfers, and even some threading can be removed to further simplify the model. As a test to determine the significance of threading, simulations were performed both with and without the threads involved. The models, after removing the threads, are shown below. It is important to note that the maximum mesh significantly decreased, from 65.552 to 8.9144.

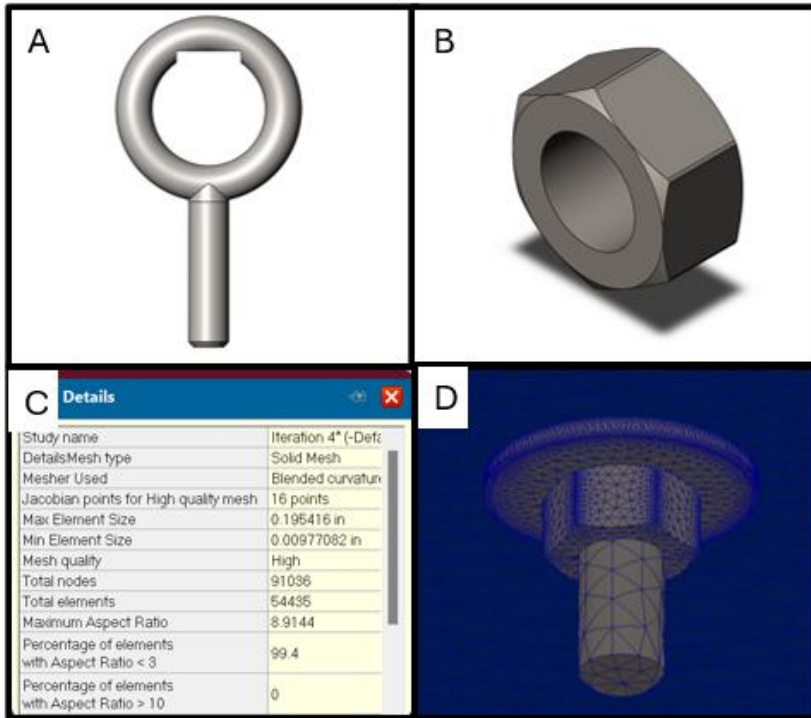
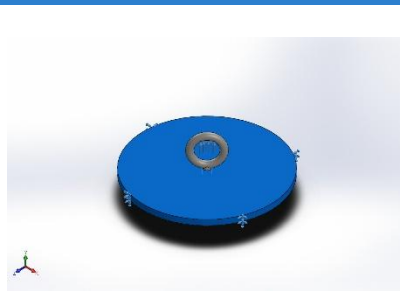


Fig. 56: A) Eyebolt Modell; B) Eyenut Model; C) Updated Meshing; D) Meshing

The model of the forward bulkhead system consisted of an AISI 304 steel eyebolt, an alloy stainless steel washer and hex nut, and the custom G10 fiberglass bulkhead material. Due to the shape of the eyebolt, a small, flat section was cut into the underside of the bulkhead, where the force was applied. Variations of this cut section were made to test the different possibilities of how our force is applied in the system.

Table 7: Material Details of Simulation Model.

Model Reference	Properties
	<p>Name: G10 Fiberglass 0 Degree Model type: Linear Elastic Isotropic Yield strength: 3.92317e+08 N/m² Elastic modulus: 7.99e+09 N/m² Poisson's ratio: 0.12 Mass density: 1,851.09 kg/m³</p>

	<p>Name: Alloy Steel (SS) Model type: Linear Elastic Isotropic Yield strength: 6.20422×10^8 N/m² Tensile strength: 7.23826×10^8 N/m² Elastic modulus: 2.1×10^{11} N/m² Poisson's ratio: 0.28 Mass density: 7,700 kg/m³</p>
	<p>Name: AISI 304 Model type: Linear Elastic Isotropic Yield strength: 2.06807×10^8 N/m² Tensile strength: 5.17017×10^8 N/m² Elastic modulus: 1.9×10^{11} N/m² Poisson's ratio: 0.29 Mass density: 8,000 kg/m³</p>

The first simulation, with the force facing directly upward, yielded a displacement of 1.067mm with a minimum FOS of 0.49. While the FOS may seem extremely low, it is important to note that this occurs over an extremely small section of the eyebolt, as shown below. The stress and strain were also quantified. While it seems like the bulkhead will have an extremely high displacement, we can see through the stress and strain that this is not the case. In fact, the system experiences very little stress and strain, meaning it can easily withstand the force applied.

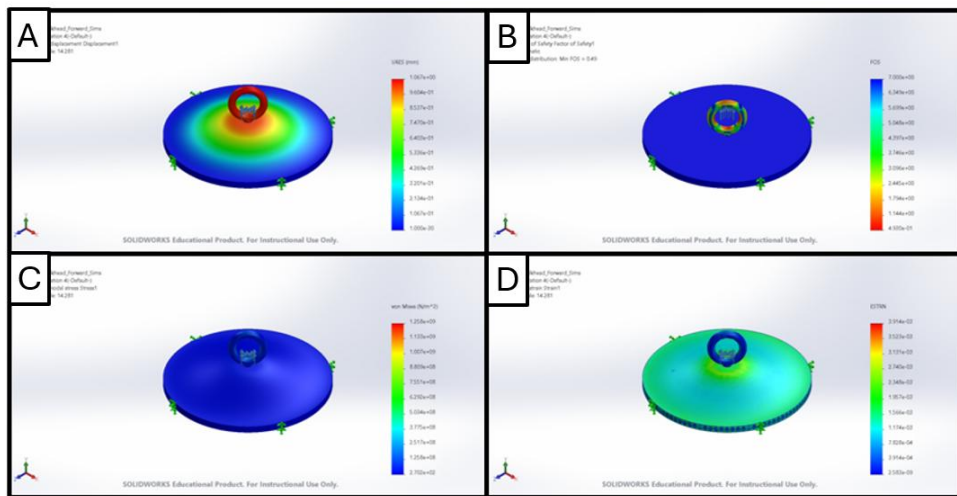


Fig. 57: A) Displacement Contour; B) Factor of Safety Contour; C) Stress Contour; D) Strain Contour

While this initial simulation was done with a perfectly vertical force, it is more realistic to assume the force can vary around the eyebolt. Therefore, to determine the worst case scenario, the angle of force application was tested at additional angles of 45 degrees and 90 degrees (parallel to the bulkhead). This helped assess the severity of several situations, and allow our team to more accurately predict what forces our system experiences under all recovery events.

The worst force possible occurred when the force was applied at a 90-degree angle from the bulkhead. The FOS on this simulation was 0.14 at a minimum and occurred at the bottom of the eyebolt.

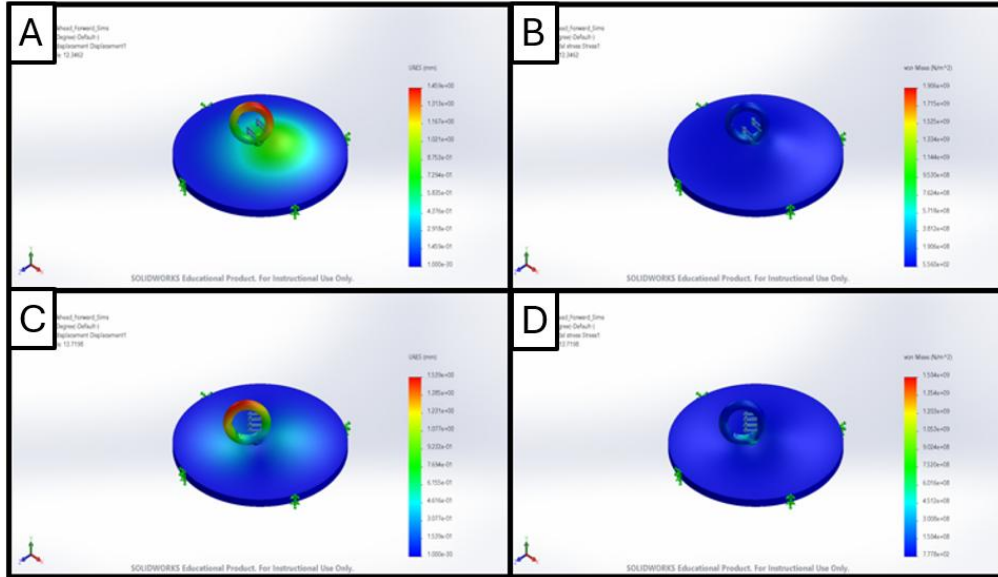


Fig. 58: A) 45 Degree Displacement; B) 45 Degree Stress; C) 90 Degree Displacement; D) 90 Degree Stress

While this is an extremely low FOS, it is important to note one item. A high force occurring on one singular point in one singular direction is highly unlikely, as the rocket has free mobility in all planes of direction. Meaning when the force is applied, the rocket will compensate accordingly. Instead, it is more realistic to assume the force will occur over time, over the entire circular area of the eyebolt. Therefore, the likelihood of the eyebolt ever experiencing a 90-degree force is near impossible.

2. Discussion

The small factor of safety occurs at small sections of the model and, notably, does not occur on the bulkheads themselves. While this may seem like a major potential concern, it is important to note that the eyebolts can easily be swapped out for higher durability/strength. The bulkheads, which are the focus of this paper, are permanently installed in the rocket, and cannot be easily removed. The FEA simulations also assume that the bulkhead itself is permanently fixed in an upwards position. However realistically, the nosecone (from where the bulkhead is attached to), has freedom in all directions. So as a force is applied, the nosecone will act accordingly, resulting in a much lower application of force on the eyebolt. Finally, while 90 degrees has the highest factor of risk, it is also impossible for this to occur in our subsystem, as the airframe is in the way, and thus the force can never directly be applied at this point. Based on these simulations, along with matching data from other sources, we can definitively say that we have confidence in our decreased bulkhead thickness, and that the bulkheads will perform nominally in all scenarios.

4. Conclusion and Further research

The simulation results offer a substantial degree of confidence in the structural integrity of our bulkhead against the forces exerted by our recovery system. However, additional testing is slated for the steel eyebolts to validate their capacity to withstand the recovery forces.

A notable aspect of this study pertains to the absence of experimentation with Poisson's ratio, and the assumption of isotropic material. To enhance the quality of our simulations, comprehensive testing of all material properties is imperative. Given the diverse fabrication methods employed in composite materials, sourcing material properties from external references may introduce inaccuracies. Moreover, the presence of anisotropic properties can significantly influence experimental outcomes and necessitates meticulous consideration during testing. While SolidWorks enables

simulation of anisotropic materials, achieving precise results across the x, y, and z directions demands extensive testing and experimentation.

An additional study for exploration involves conducting a tension test on a circular diameter section of G10, similar to our rocket bulkheads. This test aims to evaluate how a circular cross-section deforms under gradual force application. Building upon the earlier findings, it is hypothesized that the force initially acts directly upon the fibers, like the behavior observed in the 0° and 90° samples, before transitioning to a distributed force pattern resembling the behavior noted in the 45° samples.

References

- [1] Howard, Z., “How to Calculate Fin Flutter Speed,” *Peak of Flight* , Jul. 2011.
- [2] MyTechFun. (n.d.). *YouTube*. Retrieved April 14, 2025, from <https://www.youtube.com/@MyTechFun>